SOD1 is a synthetic lethal target in *PPM1D*-mutant leukemia cells

Linda Zhang[1,2,3,4,5], Joanne I. Hsu[1,2,3], Etienne D. Braekeleer[6], Chun-Wei Chen[3,4,5,7], Tajhal D. Patel[8], Hidetaka Urya[9], Anna G. Guzman[4], Alejandra G. Martell[4], Sarah M. Waldvogel[2,3,4,5,10], Ayala Tovy[3,4,5], Elsa Callen[11], Rebecca Murdaugh[3,4,5,12], Rosemary Richard[3,4,5,12], Sandra Jansen[13], Lisenka Vissers[13], Bert B.A. de Vries[13], Andre Nussenzweig[10], Shixia Huang[4,14], Cristian Coarfa[4], Jamie N. Anastas[3,4,5,12], Koichi Takahashi[9,14], George Vassiliou[6], Margaret A. Goodell*[,3,4,5]

1. Translational Biology and Molecular Medicine Graduate Program, Baylor College of Medicine, Houston, TX
2. Medical Scientist Training Program, Baylor College of Medicine, Houston, TX.
3. Stem Cells and Regenerative Medicine Center, Baylor College of Medicine, Houston TX
4. Department of Molecular and Cellular Biology, Baylor College of Medicine, Houston, TX
5. Center for Cell and Gene Therapy, Houston, TX
6. Department of Haematology, Wellcome-MRC Cambridge Stem Cell Institute, University of Cambridge
7. Integrated Molecular and Biomedical Sciences Graduate Program, Baylor College of Medicine, Houston, TX
8. Texas Children's Hospital Department of Hematology/Oncology, Baylor College of Medicine, Houston, TX
9. Department of Leukemia, The University of Texas MD Anderson Cancer Center, Houston, TX
10. Cancer and Cell Biology Graduate Program, Baylor College of Medicine, Houston, TX
11. Laboratory of Genome Integrity, National Cancer Institute, National Institute of Health, Bethesda, MD
12. Department of Neurosurgery, Baylor College of Medicine, Houston, TX
13. Donders Centre for Neuroscience, Radboud University Medical Center, Nijmegen, The Netherlands
14. Department of Education, Innovation and Technology, Advanced Technology Cores
15. Department of Genomic Medicine, The University of Texas MD Anderson Cancer Center, Houston, TX

***Corresponding Author:**
Margaret A. Goodell, Ph.D.
Professor and Chair
Department of Molecular and Cellular Biology
Director, Stem Cells and Regenerative Medicine Center
Vivian L. Smith Chair of Regenerative Medicine
Baylor College of Medicine
One Baylor Plaza, BCM N1030
Houston, TX 77030
713-798-6037
goodell@bcm.edu

Abstract

The DNA damage response is critical for maintaining genome integrity and is commonly disrupted in the development of cancer. PPM1D (protein phosphatase, Mg2+/Mn2+ dependent 1D) is a master negative regulator of the response; gain-of-function mutations and amplifications of *PPM1D* are found across several human cancers making it a relevant pharmacologic target. Here, we used CRISPR/Cas9 screening to identify synthetic-lethal dependencies of *PPM1D,* uncovering superoxide dismutase-1 (SOD1) as a potential target for PPM1D-mutant cells. We revealed a dysregulated redox landscape characterized by elevated levels of reactive oxygen species and a compromised response to oxidative stress in *PPM1D*-mutant cells. Moreover, we observed marked genomic instability in mutant cells, which is exacerbated upon inhibition of SOD1. Altogether, our results demonstrate the protective role of SOD1 against oxidative stress and DNA damage in *PPM1D*-mutant leukemia cells and highlight a new potential therapeutic strategy against *PPM1D*-mutant cancers.

Introduction

Cellular DNA is frequently damaged by both endogenous and exogenous factors (Hoeijmakers, 2009). Unresolved DNA damage can lead to genomic instability, which is a hallmark of aging and cancer (Hanahan and Weinberg, 2011). Cells have evolved intricate mechanisms to detect and repair DNA lesions. The DNA damage response (DDR) is a complex network of signaling pathways that coordinate various cellular processes initiated by p53, such as DNA repair (Ciccia and Elledge, 2010), cell cycle checkpoint activation (Harper et al., 1993), and apoptosis (Yonish-Rouach et al., 1991). However, upon resolution of DNA damage, the cell must terminate the DDR to avoid prolonged cell cycle arrest and apoptosis. One critical mechanism for DDR termination is the expression of Protein Phosphatase Mg^{2+}/Mn^{2+}–Dependent 1D (PPM1D) (Fiscella et al., 1997), which is induced by p53 and plays a key role in attenuating the response. PPM1D is a member of the PP2C family of serine/threonine protein phosphatases and has been shown to dephosphorylate a wide range of DDR signaling molecules including p53, p38 MAPK, CHK1, CHK2, and H2AX (Bulavin et al., 2002; Cha et al., 2010; Lu et al., 2005; Oliva-Trastoy et al., 2007; Takekawa et al., 2000). These dephosphorylation events generally lead to reduced activity of the targets, ultimately resulting in deactivation of the DDR.

Dysregulation of PPM1D has been associated with the development of diverse cancers, including breast, ovarian, esophagus, brain, and others (Khadka et al., 2022; Li et al., 2002; Li et al., 2020b; Ruark et al., 2013; Zhang et al., 2014). *PPM1D* is located on chromosome 17q and therefore frequently amplified in breast and ovarian cancers exhibiting 17q23 amplifications (Li et al., 2002; Ruark et al., 2013). These amplifications result in overexpression of the wildtype PPM1D protein and consequent suppression of p53 and other PPM1D targets in the DDR (Bulavin et al., 2002; Lambros et al., 2010). In addition, PPM1D can also become dysregulated through mutations in its terminal exon. These mutations produce a truncated protein that is stabilized, evading proteasome-mediated degradation (Tokheim et al., 2021). The resulting mutant protein maintains its phosphatase activity and is found at high levels even in the absence of DNA damage. Excessive PPM1D activity leads to constitutive dephosphorylation and downregulation of PPM1D targets including multiple members of the DDR (Hsu et al., 2018). These gain-of-function *PPM1D* mutations are observed in diverse solid cancers including osteosarcoma (He et al., 2021), colorectal carcinoma (Peng et al., 2014; Yin et al., 2013), diffuse midline gliomas (Wang et al., 2011; Zhang et al., 2014) and others. Moreover, *PPM1D* mutations and overexpression are associated with advanced tumor stage, worse prognosis, and increased

lymph node metastasis (Fu et al., 2014; Jiao et al., 2014; Li et al., 2020a; Li et al., 2020b; Peng et al., 2014; Zhang et al., 2014).

More recently, *PPM1D*-mutations have been shown to drive expansion of hematopoietic stem cells (Bolton et al., 2020; Hsu et al., 2018; Kahn et al., 2018) in association with clonal hematopoiesis (CH), a pre-malignant state associated with an increased risk of hematologic malignancies and elevated all-cause mortality (Genovese et al., 2014; Jaiswal et al., 2014). *PPM1D*-mutations are particularly enriched in patients with prior exposure to cytotoxic therapies, who have a high risk of therapy-related myeloid neoplasms (t-MN) (Hsu et al., 2018; Lindsley et al., 2017). Given the prevalence of *PPM1D* aberrations in cancer, PPM1D is an attractive therapeutic target. Ongoing efforts are focused on elucidating the structure of PPM1D to improve drug design and development (Miller et al., 2022). While several inhibitors thus far have shown efficacy *in vitro*, few have been studied *in vivo* and none have progressed to clinical trials due to poor bioavailability. Therefore, identifying targetable, synthetic-lethal partners to exploit the genetic defects of *PPM1D*-altered cells can offer an alternative therapeutic approach.

In this study, we performed an unbiased, whole-genome CRISPR screen to investigate genes essential for cell survival in *PPM1D*-mutated leukemia cell lines. We identified superoxide dismutase-1 (*SOD1*) as a novel synthetic-lethal dependency of PPM1D which was validated by genetic and pharmacologic approaches. We showed that the mutant cells display compromised responses to oxidative stress and DNA damage, leading to increased reactive oxygen species and genomic instability. These results provide valuable insights into the biological processes corrupted by mutant PPM1D and underscore the potential of SOD1 as a targetable vulnerability in this context.

Results

SOD1 is a synthetic lethal vulnerability of *PPM1D*-mutant leukemia cells

CRISPR dropout screens have emerged as a powerful tool to assess the functional importance of individual genes within a particular pathway by measuring the impact of their depletion on cell viability or fitness. To identify genes essential for *PPM1D*-mutant cell survival, we first created isogenic wild-type (WT) and *PPM1D*-mutant Cas9-expressing OCI-AML2 leukemia cell lines and selected two *PPM1D*-mutant clones for CRISPR screening (**Figure 1–**

figure supplement 1A). We transduced the cells with a whole-genome lentiviral library containing 90,709 guide RNAs (gRNAs) targeting 18,010 human genes (Tzelepis et al., 2016). At day ten post-transduction, the cells were harvested for the first timepoint and then subsequently passaged for an additional 18 days to allow for negatively selected gene-knockout cells to “drop out”. The remaining pool of cells were collected for deep sequencing analysis of gRNA abundance (**Figure 1A**). We analyzed genes that were specifically depleted in the mutant but not WT cells using the MaGECK-VISPR pipeline (Li et al., 2014). Differentially depleted genes are those for which the knockout or depletion of the gene results in a significant impact on the viability or growth of *PPM1D*-mutant cells compared to WT control cells. Through this analysis, we identified 409 differentially depleted genes in one of the *PPM1D*-mutant clones and 92 differentially depleted genes in the other clone while adhering to the maximum false discovery rate (FDR) cutoff of 25%. Among these genes, we found 37 common candidates that were depleted in both *PPM1D*-mutant biological replicates that were not depleted in the WT control cells **(Figure 1–figure supplement 1B, Figure 1–source data 1)**.

Gene ontology analysis of these top essential genes demonstrated an enrichment in pathways related to DNA repair, interstrand crosslink (ICL) repair, and cellular responses to stress (**Figure 1B**). Pathway analyses with the KEGG and REAC databases revealed a significant enrichment of the Fanconi anemia (FA) repair pathway, with notable genes such as *BRIP1* (*FANCJ*), *FANCI, FANCA, SLX4* (*FANCP), UBE2T* (*FANCT*), and *C19orf40 (FAAP24)* **(Figure 1–figure supplement 1C)**. Interestingly, our dropout screen revealed that superoxide dismutase 1, or *SOD1*, was the top essential gene based on fitness score (**Figure 1C**). SOD1 is a crucial enzyme involved in scavenging superoxide (O_2^-) radicals, which are harmful byproducts of mitochondrial cellular metabolism. Excessive reactive oxygen species (ROS) causes oxidative stress, which can damage cellular structures including DNA, proteins, and lipids. SOD1 is an attractive therapeutic target due to the availability of SOD1 small molecule inhibitors that are being tested in clinical trials (Lin et al., 2013; Lowndes et al., 2008). Therefore, we decided to further investigate the role of SOD1 in promoting *PPM1D*-mutant cell survival.

To validate the essentiality of SOD1 in *PPM1D*-mutant cells, we performed *in vitro* competitive proliferation assays in two different acute myeloid leukemia (AML) cell lines, OCI-AML2 and OCI-AML3. We transduced isogenic WT and *PPM1D*-mutant Cas9-expressing cells with either empty vector (EV) or two different *SOD1*-gRNA-expressing lentiviral vectors containing a blue-fluorescent protein (BFP) reporter. While loss of *SOD1* had minimal effects on the fitness

of WT cells, *PPM1D*-mutant cells with *SOD1* deletion had significant reduction in cellular growth in both OCI-AML2 and OCI-AML3 cells (**Figure 1D**). Collectively, these results show that loss of *SOD1* confers a significant disadvantage specific to *PPM1D*-mutant leukemia cells.

***PPM1D*-mutant cells are sensitive to SOD1 inhibition and have increased oxidative stress**

We next wanted to test if pharmacologic inhibition of SOD1 could mimic the genetic deletion of *SOD1*. We used two different SOD1 inhibitors, Lung Cancer Screen-1 (LCS-1) and *Bis*-choline tetrathiomolybdate (ATN-224), which work by different mechanisms. LCS-1 is a small molecule that binds to SOD1 and disrupts its activity (Somwar et al., 2011), while ATN-224 is a copper chelator that reduces SOD1 activity by decreasing the availability of copper ions, which are an essential SOD1 cofactor (Juarez et al., 2006). To study the sensitivity of *PPM1D*-mutant cells to SOD1 inhibition, we engineered three patient-derived AML cell lines, MOLM-13, OCI-AML2, and OCI-AML3 which harbor distinct genetic backgrounds and AML driver mutations. Upon treatment with either ATN-224 or LCS-1, we found that SOD1 inhibition induced a significantly greater proportion of apoptotic *PPM1D*-mutant than *PPM1D*-WT cells (**Figure 2–figure supplement 1A**). *PPM1D*-truncating mutations conferred significant sensitivity to SOD1 inhibition compared to their WT counterparts in all three AML cell lines **(Figure 2A, Figure 2–figure supplement 1B**). To determine if this cytotoxicity was dependent on oxidative stress, we treated the cells with SOD1 inhibitors in combination with an antioxidant, N-acetylcysteine (NAC). Importantly, NAC supplementation was able to completely rescue the sensitivity of mutant cells to both LCS-1 and ATN-224 treatment (**Figure 2B, Figure 2–figure supplement 1C**), suggesting that ROS generation contributes to the sensitivity of mutant cells to SOD1 inhibition.

Activating mutations in oncogenes often lead to increased ROS generation by altering cellular metabolism, inducing replication stress, or dysregulating redox homeostasis (Maya-Mendoza et al., 2015; Park et al., 2014). We therefore hypothesized that *PPM1D*-mutant cells have increased oxidative stress, leading to reliance on SOD1 for protection. SOD1 catalyzes the breakdown of superoxide into hydrogen peroxide and water. Therefore, we first assessed mitochondrial superoxide levels using the fluorogenic dye, Mitosox Green. This mitochondrial-targeted dye is rapidly oxidized by superoxide, but not other types of ROS, to produce green fluorescence. We observed that in the absence of exogenous stressors, *PPM1D*-mutant cells had a moderate increase in superoxide radicals (**Fig. 2C**). Free radicals can be detrimental to cells

due to their ability to oxidize proteins, lipids, and DNA. Therefore, we also measured levels of lipid peroxidation as an additional measure of oxidative stress. Consistent with the increase in superoxide radicals, we observed a concurrent increase in lipid peroxidation in the *PPM1D*-mutant cells **(Figure 2D**). Using 2'7'-dichlorofluorescein diacetate (DCFDA) staining to measure total ROS levels, we observed that *PPM1D*-mutant cells harbored more total ROS compared to WT cells and that upon inhibition of SOD1, there was an increase in ROS that was specific to the mutant cells (**Figure 2E**).

To investigate whether the observed elevated ROS was a characteristic of other *PPM1D*-mutant cell lines, we measured ROS levels in two different germline models. Humans with germline mutations in *PPM1D* were first described by Jansen et al. in 2017 in patients with intellectual disability. This neurodevelopmental condition is named Jansen-de Vries syndrome (JdVS, OMIM #617450) and is characterized by frameshift or nonsense mutations in the last or second-to-last exons of the *PPM1D* gene. These mutations result in functionally active, truncated mutant proteins like those exhibited in human cancers and clonal hematopoiesis. Lymphoblastoid cell lines (LCLs) were generated from these JdVS patients by Jansen et al (Jansen et al., 2017; Wojcik et al., 2023). In addition to human *PPM1D*-mutant LCLs, we also generated mouse embryonic fibroblasts (MEFs) from a germline mouse model harboring a heterozygous truncating mutation in the terminal exon of *Ppm1d (Hsu et al., 2018)*. When we measured total ROS from both the JdVS LCLs and the *Ppm1d*-mutant MEFs compared to their WT counterparts, both mutant models exhibited greater levels of total ROS (**Figure 2–figure supplement 1D, E**). Additionally, *PPM1D*-mutant LCLs were also more sensitive to pharmacologic SOD1 inhibition compared to the WT LCL line, GM12878 (**Figure 2–figure supplement 1F**). These results demonstrate that *PPM1D* mutations not only increase ROS in the context of cancer, where cellular metabolism is often altered, but can also alter redox homeostasis in non-transformed cells.

To determine if mutant PPM1D was associated with ROS generation, we treated isogenic OCI-AML2 WT and *PPM1D*-mutant cells with a PPM1D inhibitor, GSK2830371, for 24 hours. We found that pharmacologic inhibition of PPM1D mildly decreased ROS levels in both WT and *PPM1D* mutant cells (**Figure 2F**), suggesting a link between PPM1D and ROS production. Altogether, these data demonstrate that SOD1 inhibition leads to preferential cytotoxicity in the mutant cells due to increased oxidative stress induced by mutant PPM1D.

226 ## *PPM1D*-mutant leukemia cells have altered mitochondrial function

227 Mitochondria are the primary source of ROS within the cell, as the electron transport chain
228 is a major site of ROS production during oxidative phosphorylation. We next asked whether the
229 observed increase in ROS in *PPM1D*-mutant cells was due to differences in mitochondrial
230 abundance. We used two independent methods to measure mitochondrial mass, including
231 MitoTracker Green flow cytometry (**Figure 3A**) and western blot analysis of mitochondrial
232 complex proteins (**Figure 3B**). However, we did not observe a difference in mitochondrial mass
233 with either method. This finding suggests that mechanisms other than a change in mitochondrial
234 abundance are responsible for the increase in ROS levels in mutant cells, such as alterations in
235 mitochondrial metabolism or changes in ROS scavenging systems.
236
237 To assess mitochondrial function, we performed seahorse assays in WT and *PPM1D*-
238 mutant OCI-AML2 cells. Our seahorse assays revealed that the mutant cells have decreased
239 mitochondrial respiration, as indicated by decreased basal, maximal, and ATP-linked respiration
240 (**Figure 3C**). While *PPM1D*-mutant MOLM-13 and OCI-AML3 cells also had decreased basal
241 respiration, there were variable differences in maximal and ATP-linked respiration compared to
242 WT, suggesting possible cell line differences affecting mitochondrial respiration **(Figure 3–figure**
243 **supplement 1A, B**). In addition to analyzing respiratory capacity, we also examined
244 mitochondrial membrane potential (MMP) using the fluorescent dye Mitotracker CMXRos, which
245 accumulates in the mitochondria in an MMP-dependent manner. We stained both WT and mutant
246 cells with Mitotracker CMXRos and observed a decrease in MMP in the mutant cells (**Figure 3D**).
247 Tracking cell numbers between the WT and mutant cell lines over time established this decrease
248 in MMP was not due to altered cellular growth rates (**Figure 3–figure supplement 1C**). Altogether,
249 these findings, along with decreased respiratory capacity and increased mitochondrial ROS,
250 indicate a mitochondrial defect in *PPM1D*-mutant cells.
251

252 ## *PPM1D*-mutant cells have a reduced oxidative stress response

253 Mitochondrial dysfunction and increased ROS production are closely intertwined. On one
254 hand, mitochondrial dysfunction leads to increased ROS production as a result of impaired
255 oxidative phosphorylation and increased electron leakage (Turrens, 2003). On the other hand,
256 sustained oxidative stress can directly damage mitochondrial components and mtDNA and
257 compromise their function (Wallace, 2005). To better understand the molecular basis for the
258 observed mitochondrial dysfunction and dependency on SOD1, we performed bulk RNA-

sequencing (RNA-seq) on Cas9-expressing WT and *PPM1D*-mutant OCI-AML2 cells transduced with *SOD1*-sgRNA to induce *SOD1* deletion or the empty vector (EV) control (**Figure 4–figure supplement 1A**). Both EV and SOD1-sgRNA vectors were tagged with a BFP reporter to identify transduced cells. The cells were collected ten-days post-transduction, the timepoint at which we observed 50% reduction of the *SOD1*-deletion cells during the *in vitro* proliferation assays, reasoning this would capture the effects of *SOD1*-deletion on cellular and metabolic processes while avoiding excessive cell death.

Analysis of the RNA-seq data revealed 3530 differentially expressed genes, with 2028 downregulated genes and 1502 upregulated genes in the mutant cells compared to WT cells at baseline (**Figure 4–source data 1**). Gene set enrichment analysis (GSEA) of the differentially expressed genes showed an upregulation in genes related to cell cycle (GO: 0007049), cell division (GO: 0051301), DNA replication (GO: 005513), and mitophagy (GO: 0000423) in the *PPM1D*-mutant cells (**Figure 4A**). Interestingly, there was a significant downregulation of pathways related to the regulation of the oxidative stress response (GO: 1902882, **Figure 4–figure supplement 1B**), ROS metabolic processes (GO: 0072593), and oxidation reduction (GO: 0055114).

Following *SOD1* deletion, the WT cells displayed notable upregulation of pathways associated with cell cycling, chromosome organization, cell division, and DNA repair. In contrast, the mutant cells showed significant downregulation of these same pathways (**Figure 4–figure supplement 1C**). Intriguingly, upon *SOD1* deletion, the mutant cells exhibited an upregulation in the response to oxidative stress (GO:0006979, **Figure 4–figure supplement 1D**). This finding suggests a reactive transcriptional response to the heightened ROS levels resulting from the loss of SOD1.

As PPM1D is a phosphatase that can directly modulate the activation state of proteins, we examined whether there were alterations in protein and phosphoprotein levels in *PPM1D*-mutant cells using reverse phase protein array (RPPA) analysis, mirroring the experimental design used for bulk RNA-seq (**Figure 4–figure supplement 1A**). By focusing on differential protein expression between wild-type (WT) and *PPM1D*-mutant cells, we aimed to capture the post-translational regulatory events that could contribute to the mitochondrial dysfunction observed in the mutants. The RPPA analysis of over 200 (phospho-)proteins covering major signaling pathways identified 128 differentially expressed proteins between *PPM1D*-mutant and control WT

OCI-AML2 cells (a panel of 264 proteins), with 67 downregulated proteins and 61 upregulated proteins (**Figure 4–figure supplement 2A, source data 2**). Notably, over-representation analysis showed that among the differentially expressed proteins, there was a significant enrichment in the "Response to Oxidative Stress" pathway in the mutant cells (-log10(pValue) = 24.164) compared to WT, with a particular emphasis on the downregulated proteins of this pathway (-log10(pValue 15.457, **Figure 4B**, **Figure 4–source data 3**). While the RNA-seq suggested a transcriptional upregulation of the response to oxidative stress in the mutant cells after *SOD1* deletion, the RPPA data revealed that the mutant cells continued to exhibit decreased expression in proteins associated with the oxidative stress response (**Figure 4–figure supplement 2B**). Taken together, these findings suggest that *PPM1D*-mutant cells have an inherent impairment in their baseline response to oxidative stress.

To further explore the diminished oxidative stress response in the mutant cells, we assessed their total- and small-molecule-antioxidant capacity. Total antioxidant capacity refers to the overall ability of the cells to counteract free radicals and reduce oxidative damage. This includes enzymatic antioxidants such as catalase, SODs, and peroxidases. Small molecule antioxidant capacity measures the capacity of low molecular weight antioxidants, such as glutathione and vitamin E, to neutralize ROS (Hawash et al., 2022). Our results showed that *PPM1D*-mutant cells have significantly reduced total and small-molecule antioxidant capacity compared to WT cells (**Figure 4C**). We also measured the protein levels of key antioxidant enzymes by western blot. While we saw similar protein levels of SOD1 in both WT and mutant cells, we observed a mild reduction in the thioredoxin and catalase levels (**Figure 4D**). These results provide evidence to support the RNA-seq and RPPA findings that *PPM1D*-mutant cells have impaired antioxidant defense mechanisms, leading to an elevation in ROS levels and reliance on SOD1 for protection.

***PPM1D* mutations increase genomic instability and impair non-homologous end-joining repair**

In addition to a decreased response to oxidative stress, the RNA-seq GSEA analysis also revealed differential responses to DNA repair. Upon *SOD1* deletion, WT cells significantly upregulated the regulation of DNA repair (GO:0006281), double-stranded break repair (GO:0006302), homologous recombination (GO:0035825), and more. However, there was a striking downregulation of DNA repair pathways after deletion of *SOD1* in the mutant cells (**Figure**

326 **4–figure supplement 1C**). PPM1D plays a key role in suppressing the DNA damage response
327 (DDR) by dephosphorylating, thereby inactivating, p53 and other key upstream and downstream
328 effectors of the pathway. Truncating mutations and amplifications in *PPM1D* that lead to increased
329 PPM1D activity may therefore inhibit DNA damage repair and increase genomic instability.
330 Oxidative stress and ROS also pose endogenous challenges to genomic integrity. Therefore, we
331 hypothesized that due to the increase in ROS within the mutant cells, loss of *SOD1* may lead to
332 unsustainable accumulation of DNA damage and overwhelm the mutant cell's DNA repair
333 capacity.
334
335 To test this hypothesis, we first sought to establish the baseline levels of DNA damage in
336 *PPM1D*-altered cells. We performed alkaline comet assays in mouse embryonic fibroblasts and
337 found a significant increase in single- and double-stranded DNA breaks in mutant cells compared
338 to WT (**Figure 5A**). we also performed metaphase spreads in mouse primary B-cells to investigate
339 chromosomal aberrations, which are consequences of abnormal double-stranded break repair.
340 WT and *Ppm1d*-mutant mouse primary resting CD43+ B-cells were purified from spleens and
341 stimulated with LPS, IL-4, and CD180 to induce proliferation. The cells were then treated with
342 either low- or high-dose cisplatin for 16-hours. Consistent with our comet assay findings, we
343 observed that *Ppm1d*-mutant cells harbored approximately two-fold more chromosomal breaks
344 per metaphase after exposure to cisplatin (**Figure 5B**). When we classified the chromosomal
345 aberrations into subtypes, we observed that the mutant cells had increased numbers of each type
346 of aberration. These results demonstrate that mutations in *PPM1D* increase genomic instability.
347
348 To further assess the DNA repair efficiency of *PPM1D*-mutant cells, we utilized U2OS
349 DNA repair reporter cell lines which express a green fluorescent protein (GFP) cassette when
350 specific DNA repair pathways are active after stimulation when the I-SceI restriction enzyme is
351 induced to stimulate a double-stranded break (DSB). To test for homologous recombination (HR),
352 tandem defective GFP genes can undergo HR to generate GFP+ cells. Non-homologous end
353 joining (NHEJ) repairs a defective GFP in a distinct cassette (Weinstock et al., 2006). Because
354 the U2OS parental line harbors an endogenous heterozygous *PPM1D* truncating mutation
355 (R458X), we corrected the lines to generate the isogenic *PPM1D* WT control (**Figure 5–figure**
356 **supplement 1A**).
357
358 With two isogenic clones for each reporter cell line, we transfected the *PPM1D*-WT and -
359 mutant U2OS clones with I-SceI and measured GFP expression by flow cytometry after 48 hours.

360 Our results showed similar levels of repair via HR in both WT and mutant clones (**Figure 5C**).
361 This finding is consistent with prior studies showing that PPM1D promotes HR by forming a stable
362 complex with BRCA1-BARD1, thereby enhancing their recruitment to DSB sites (Burdova et al.,
363 2019). In contrast, we saw significantly decreased NHEJ repair in the *PPM1D*-mutant clones
364 (**Figure 5D**). Prior studies have shown that PPM1D modulates lysine-specific demethylase 1
365 (LSD1) activity, which is important for facilitating the recruitment of 53BP1 to DNA damage sites
366 through RNF168-dependent ubiquitination (Peng et al., 2015). PPM1D mutations may therefore
367 lead to impairment of NHEJ through dysregulation of 53BP1 recruitment. To confirm this, we
368 performed immunofluorescence imaging of Rad51 and 53BP1 foci. The recruitment of Rad51 and
369 53BP1 to the sites of DNA damage are important for the activation of HR and NHEJ, respectively.
370 We analyzed mouse embryonic fibroblasts at baseline and after irradiation (10 Gy) and observed
371 similar numbers of Rad51 foci in *Ppm1d*-mutant and WT cells (**Figure 5–figure supplement 1B**).
372 In contrast, *Ppm1d*-mutant MEFs had fewer 53BP1 foci, indicating decreased NHEJ repair
373 capacity that was consistent with our U2OS reporter line findings (**Figure 5–figure supplement**
374 **1C**). Comet assays were performed in parallel with the immunofluorescence experiments to show
375 that the mutant cells had increased DNA damage (**Figure 5–figure supplement 1D**). Therefore,
376 the decrease in foci was not due to resolution of DNA damage, but rather due to inefficient DNA
377 repair.
378
379 Lastly, to investigate the impact of SOD1 inhibition on DNA damage, we treated cells with
380 a SOD1 inhibitor and performed comet assays. Consistent with our earlier observations, *PPM1D*-
381 mutant cells exhibited a higher burden of DNA breaks. Upon treatment with ATN-224, the mutant
382 cells displayed a significant increase in DNA damage compared to their baseline levels, while the
383 WT cells maintained relatively stable levels of DNA damage (**Figure 5E**). As ROS are known to
384 contribute to oxidative DNA damage, we further assessed the levels of 8-oxo-2′-deoxyguanosine
385 (8-Oxo-dG), a well-established marker of oxidative DNA damage. Strikingly, the mutant cells
386 demonstrated elevated levels of oxidative DNA damage both at baseline and following SOD1
387 inhibition with ATN-224, whereas the WT cells once again did not exhibit a substantial increase
388 in oxidative DNA damage upon treatment with ATN-224 (**Figure 5F**). Collectively, these findings
389 demonstrate that inhibiting SOD1 in *PPM1D*-mutant cells exacerbates DNA damage, ultimately
390 contributing to death of the *PPM1D*-mutant cells.

Discussion

The search for synthetic-lethal strategies for cancer therapy has gained significant attention in recent years due to the potential to identify new therapeutic targets that exploit tumor-specific vulnerabilities. In this study, we utilized whole-genome CRISPR/Cas9 screening to uncover synthetic-lethal vulnerabilities of *PPM1D*-mutant leukemia cells. Our screen revealed that the top essential gene in *PPM1D*-mutant cells was *SOD1*. We investigated the mechanisms underlying this dependency and characterized the redox landscape of *PPM1D*-mutant cells, which revealed significant oxidative stress and mitochondrial dysfunction. Recent studies have suggested that PPM1D is indirectly associated with energy metabolism via dephosphorylation of the ataxia telangiectasia mutated (ATM) protein. ATM promotes mitochondrial homeostasis, and therefore sustained inactivation of ATM could lead to potential mitochondrial dysfunction (Bar et al., 2023; Guleria and Chandna, 2016). However, oxidative stress and mitochondrial dysfunction are closely related, and it is difficult to dissect the driving factor. We therefore performed RNA-sequencing and RPPA analysis to better understand the underlying processes contributing to the heightened oxidative stress observed in the mutant cells. Our analyses indicated a diminished response to oxidative stress in the mutant cells. These findings may suggest a self-amplifying cycle whereby dysregulation of ROS scavenging systems increases ROS levels, which in turn leads to mitochondrial dysfunction, which further exacerbates oxidative stress. Hence, the additional impairment of ROS detoxification mechanisms within the cell, such as the loss of SOD1, has detrimental consequences for the viability of mutant cells.

Multiple mechanisms may underlie the suppressed oxidative stress response observed in *PPM1D*-mutant cells. One possible explanation is through PPM1D-mediated inhibition of p53. p53 exhibits complex and context-dependent roles in cellular responses to oxidative stress, and its functions can vary depending on the severity of stress encountered by the cell (Kang et al., 2013; Liang et al., 2013; Sablina et al., 2005). Under mild or moderate oxidative stress conditions, p53 may protect the cell from ROS by inducing the transcription of genes such as superoxide dismutase (SOD), glutathione peroxidase (GPx), and others (Dhar et al., 2011; Peuget et al., 2014; Sablina et al., 2005; Tan et al., 1999). However, under severe or prolonged oxidative stress, the pro-apoptotic functions of p53 may promote ROS production to eliminate cells that have accumulated excessive DNA damage or irreparable cellular alterations. The duality of these anti- and pro-oxidant functions of p53 highlight its intricate role in modulating responses to oxidative stress. How PPM1D affects the switch between these functions of p53 is not understood. Furthermore, the extent to which the dependency on SOD1 observed in *PPM1D*-mutant cells is

425 mediated through p53 remains unclear and requires deeper exploration to better understand the
426 context in which SOD1 inhibitors can be used in cancer therapy.
427
428 Oxidative stress and DNA damage are intimately linked processes that frequently co-occur.
429 Our study also investigated the interplay between PPM1D, DNA damage, and oxidative stress.
430 We demonstrated significant genomic instability of *PPM1D*-mutant cells at baseline and further
431 characterized the effects of mutant PPM1D on specific DNA repair pathways. While previous
432 studies have suggested a role for PPM1D in modulating HR and NHEJ (Burdova et al., 2019;
433 Peng et al., 2015), our study is the first to demonstrate impaired NHEJ in *PPM1D*-mutant cells.
434 Additionally, our study corroborated previous research demonstrating the synthetic-lethal
435 relationship of *SOD1* and other DNA damage genes such as *RAD54B, BLM,* and *CHEK2 (Sajesh*
436 *et al., 2013; Sajesh and McManus, 2015)*. In the context of *PPM1D* mutations, we showed that
437 SOD1 inhibition amplifies oxidative stress and DNA damage, ultimately culminating in mutant cell
438 death. These findings align with previous studies demonstrating that the inhibition of SOD1 by
439 LCS-1 leads to the degradation of key DNA repair proteins, PARP1 and BRCA1, resulting in ROS-
440 dependent death of glioma cells (Ling et al., 2022). Similar observations were made in colorectal
441 cancer models, where LCS-1 treatment enhanced the effectiveness of PARP1 inhibition. These
442 results highlight the potential of combinatorial therapies to achieve therapeutic synergism and
443 underscores the intricate relationship between ROS and DNA damage.
444
445 Interestingly, our screen also uncovered sensitivity of *PPM1D*-mutant cells to dropout of
446 genes in the Fanconi Anemia (FA) DNA repair pathway including *BRIP1* (*FANCJ*), *FANCI,*
447 *FANCA, SLX4* (*FANCP), UBE2T* (*FANCT*), and *C19orf40 (FAAP24).* The FA pathway plays a
448 crucial role in facilitating the repair of interstrand crosslinks by coordinating the recruitment of
449 various DNA repair pathways, such nucleotide excision repair, translesion synthesis, and
450 homologous recombination (Ceccaldi et al., 2016; Kottemann and Smogorzewska, 2013).
451 Furthermore, the FA genes are also essential for safeguarding genomic integrity during replication
452 stress by protecting replication forks (Schlacher et al., 2012). Previous studies have highlighted
453 the essentiality of the FA pathway in p53-deficient cells (Ardeljan et al., 2020). Another study also
454 showed that several FA pathway genes are shared synthetic-lethal partners in cells with various
455 loss of tumor suppressors including *PBRM1, LKB1, TP53, TP53BP1*, and *CHD1* (Feng et al.,
456 2022). In the context of cancer, cells with defects in DNA repair mechanisms heavily rely on
457 compensatory pathways for survival. A prominent example is the successful treatment of
458 BRCA1/2-deficient breast cancers with PARP1 inhibitors (50, 51). Given the observed

suppression of p53 and increased genomic instability, it is reasonable that the FA pathway is also a dependency in *PPM1D*-mutant cells. However, the lack of small molecule inhibitors specifically targeting the FA pathway hinders our ability to directly assess its therapeutic potential in targeting *PPM1D*-mutant cells in our study.

In summary, our investigation sheds light on the role of mutant PPM1D in modulating cellular responses to oxidative stress and DNA repair in leukemia cells, offering valuable insights into the underlying molecular mechanisms. This research not only enhances our understanding of PPM1D-mediated cellular responses, but also identifies potential therapeutic targets against *PPM1D*-mutant leukemia cells. However, it is important to acknowledge the limitations of our study. We recognize that while *PPM1D* mutations are frequently observed in patients with t-MN, they are rare in *de novo* AML (Hsu et al., 2018). While there is ample evidence that *PPM1D* is an oncogenic driver in many types of cancers (Ali et al., 2012; Khadka et al., 2022; Li et al., 2002; Nguyen et al., 2010; Wu et al., 2016), the clinical importance of targeting pre-malignant PPM1D-associated clonal expansion in the hematopoietic system is not clear. However, the prevalence of *PPM1D* somatic mutations in other tissues such as the esophagus, suggests the need for further investigation (Yokoyama et al., 2019).

Materials and Methods

Cell lines and Reagents

Cas9-expressing OCI-AML2 cells were generated by lentiviral transduction using pKLV2-EF1aBsd2ACas9-W plasmid obtained from Dr. Kosuke Yusa from the Sanger Institute (Addgene #67978). Four days post-transduction, cells underwent blasticidin selection. Single clones were obtained by fluorescence-activated cell sorting and functionally tested for Cas9 activity using a lentiviral reporter pKLV2-U6gRNA5(gGFP)-PGKBFP2AGFP-W (Addgene #67980). *PPM1D*-mutant cell lines were generated using the RNP-based CRISPR/Cas9 delivery method using a single sgRNA (GCTAAAGCCCTGACTTTA). Two *PPM1D*-mutant clones were validated and selected for the CRISPR dropout screen.

CRISPR Dropout Screen and Analyses

For large-scale production of lentivirus, 15 cm plates of 80-90% confluent 293T cells were transfected using Lipofectamine 2000 (Invitrogen) with 7.5 ug of the Human Improved Whole-Genome Knockout CRISPR library V1 (by Kosuke Yuya, Addgene #67989), 18.5 ug of psPax2, and 4 ug of pMD2.G. For the CRISPR dropout screen, one WT and two independent *PPM1D* mutant Cas9-expressing OCI-AML2 cell lines were used as biological replicates, with three technical replicates per line. 3 x 10^7 cells were transduced with the lentivirus library supernatant. Three days post-transduction, the cells were selected with puromycin for three days. Cells were collected on day 28 for genomic DNA isolation using isopropanol precipitation. Illumina adapters and barcodes were added to samples by PCR as previously described (Tzelepis et al., 2016). Single-end sequencing was performed on the HiSeq 2000 V4 platform and cell-essential genes were identified using the MaGECK-VISPR (Li et al., 2014).

Competitive Proliferation Assay

Gene-specific sgRNAs were cloned into the pKLV2-U6gRNA5(BbsI)-PGKpuro2ABFP (Addgene #67974) lentiviral backbone. 293T cells (0.4 x 10^6 cells per well) were seeded in a six-well plate the day prior and transfected using lipofectamine 3000 with pMD2G (0.8 ug), pAX2 (1.6 ug), and the sgRNA-BFP (1.6 ug) plasmids. Cas9-expressing cells were then seeded in 12-well plates (200k cells per well, in triplicates) in media supplemented with 8ug/ml polybrene and 5 ug/mL blasticidin, and lentivirally transduced at a titer that yields 50% infection efficiency. Cells were assayed using flow cytometry for BFP expression between 4- and 16-days post-transduction and normalized to the BFP percentage at day 4.

Drug and Proliferation Assays

Drug and proliferation assays were done using the Cell Proliferation MTT Kit (Sigma) as per manufacturer's protocol. Briefly, 1 x 10^4 cells were plated in 96-well, flat bottom plates and treated with vehicle or drugs in a total volume of 100 uL. Plates were incubated at 37ºC for at least 24 hours. 10 uL of MTT labeling reagent was added to each well and incubated for 4 hours. 100 uL of solubilization buffer was added to each well and incubated overnight. Plates were analyzed using a fluorometric microplate reader at 550 nm.

520 **Alkaline Comet Assay**
521 Comet assays were conducted as previously described (Greve et al., 2012; Schmezer et al.,
522 2001). Cells were resuspended to 1 x 10^5 cells/mL and mixed with 1% low-melting agarose (R&D
523 Systems) at a 1:10 ratio and plated on 2-well comet slides (R&D Systems). Cells were then lysed
524 overnight and immersed in alkaline unwinding solution as per manufacturer's protocol (Trevigen).
525 Fluorescence microscopy was performed at 10X magnification using the Keyence BZ-X800
526 microscope and analyses of comet tails were performed using the Comet Assay IV software
527 (Instem). At least 150 comet tails were measured per sample.
528
529 **Chromosome aberration analysis mitotic chromosome spreads**
530 Primary resting mouse splenic B-cells were isolated using anti-CD43 microbeads (Miltenyi Biotec)
531 and activated with 25 ug/mL LPS (Sigma), 5 ng/mL IL-4 (Sigma), and 0.5 ug/mL anti-CD180 (BD
532 Pharmingen) for 30 hours. The cells were then treated with cisplatin for 16 hours at two
533 concentrations - 0.5 uM and 5 uM cisplatin. Metaphases were prepared as previously described
534 (Zong et al., 2019). Briefly, cells were arrested at mitosis with colcemid (0.1 ug/mL, ThermoFisher)
535 for 1 hour. Cells were then incubated in a prewarmed, hypotonic solution of potassium chloride
536 (75 mM) for 20 minutes to induce swelling and fixed in methanol/glacial acetic acid (3:1). Droplets
537 were spread onto glass slides inside a cytogenetic drying chamber. Fluorescence *in situ*
538 hybridization was performed using a Cy3-labeled peptide nucleic acid probe to stain telomeres
539 and DNA was counterstained by DAPI. At least 50 metaphases were scored for chromosome
540 aberrations for each experimental group.
541
542 **ROS Assays**
543 To measure superoxide, total cellular reactive oxygen species (ROS), and lipid peroxidation, 1 x
544 10^6 cells were collected after the indicated treatments and washed with PBS. The cells were
545 stained with 1 uM Mitosox Green (Thermofisher), 20 uM 2'7'-dichlorofluorescin diacetate (DCFDA,
546 Abcam), or 2.5 uM BODIPY 581/591 (Thermofisher) in FBS-free Hanks' buffered saline solution
547 (HBSS, Thermofisher), and incubated at 37ºC for 30 minutes. The staining was quenched with
548 complete HBSS (2% FBS, 1% HEPES) and washed twice before being resuspended in DAPI-
549 containing PBS to assess ROS in viable cells. The data was acquired using an LSRII (BD
550 Biosciences) and analyzed on Flowjo.
551
552 **Reverse-Phase Protein Array**
553 Reverse phase protein array assays for antibodies to proteins or phosphorylated proteins in
554 different functional pathways were carried out as described previously (Coarfa et al., 2021; Lu H.-
555 Y., 2021; Wang et al., 2022). Specifically, protein lysates were prepared from cultured cells with
556 modified Tissue Protein Extraction Reagent (TPER) (Life Technologies Corporation, Carlsbad,
557 CA) and a cocktail of protease and phosphatase inhibitors (Roche, Pleasanton, CA) (Lu et. al.
558 2021). The lysates were diluted into 0.5 mg/ml in SDS sample buffer and denatured on the same
559 day. The Quanterix 2470 Arrayer (Quanterix, Billerica, MA) with a 40 pin (185 µm) configuration
560 was used to spot samples and control lysates onto nitrocellulose-coated slides (Grace Bio-labs,
561 Bend, OR) using an array format of 960 lysates/slide (2880 spots/slide). The slides were
562 processed as described and probed with a set of 264 antibodies against total proteins and
563 phosphoproteins using an automated slide stainer Autolink 48 (Dako, Santa Clara, CA). Each

slide was incubated with one specific primary antibody and a negative control slide was incubated with antibody diluent without any primary antibody. Primary antibody binding was detected using a biotinylated secondary antibody followed by streptavidin-conjugated IRDye680 fluorophore (LI-COR Biosciences, Lincoln, NE). Total protein content of each spotted lysate was assessed by fluorescent staining with Sypro Ruby Protein Blot Stain according to the manufacturer's instructions (Molecular Probes, Eugene, OR).

Fluorescence-labeled slides were scanned on a GenePix 4400 AL scanner, along with accompanying negative control slides, at an appropriate PMT to obtain optimal signal for this specific set of samples. The images were analyzed with GenePix Pro 7.0 (Molecular Devices, Silicon Valley, CA). Total fluorescence signal intensities of each spot were obtained after subtraction of the local background signal for each slide and were then normalized for variation in total protein, background and non-specific labeling using a group-based normalization method as described (Lu H.-Y., 2021). For each spot on the array, the-background-subtracted foreground signal intensity was subtracted by the corresponding signal intensity of the negative control slide (omission of primary antibody) and then normalized to the corresponding signal intensity of total protein for that spot. Each image, along with its normalized data, was evaluated for quality through manual inspection and control samples. Antibody slides that failed the quality inspection were either repeated at the end of the staining runs or removed before data reporting. A total of 261 antibodies remained in the list. Multiple t-tests with Benajimini Hochberg correction were performed for statistical analysis and filtering was based on an FDR <0.2 and linear fold change of >1.25.

RNA-sequencing

Bulk RNA-sequencing was performed on WT and *PPM1D*-mutant OCI-AML2 cells after lentiviral *SOD1* CRISPR knockout. Cells were transduced with pKLV2-U6-sgRNA-BFP lentivirus (either empty vector or with *SOD1*-sgRNA). Transduced cells were then cultured for 10 days and BFP+ cells were sorted directly into Buffer RLT Plus with ß-mercaptoethanol. RNA was isolated using the Allprep DNA/RNA Micro Kit (Qiagen) per manufacturer's protocols. RNA-sequencing library preparation was done using the True-Seq Stranded mRNA kit (Illumina) per manufacturer's protocol. Quality control of libraries was performed using a TapeStation D1000 ScreenTape (Agilent, 5067-5584). Libraries were then sequenced using an Illumina Nextseq 2000 sequencer, aiming for >20 million reads per biological replicate. Paired-end RNA-sequencing reads were obtained. obtained and trimmed using trimGalore (https://github.com/FelixKrueger/TrimGalore). Mapping was performed using the STAR package (Dobin et al., 2013) against the human genome build UCSC hg38 and counts were quantified with featureCounts (Liao et al., 2014). Differential expression analysis was performed using the DESeq2 R package (1.28.1) (Love et al., 2014). P-values were adjusted with Benjamini and Hochberg's approach for controlling the false discovery rate (FDR). Significant differentially expressed genes between the indicated comparisons were filtered based on an FDR< 0.05 and absolute fold change exceeding 1.5.

Seahorse Assay

Mitochondrial bioenergetics in AML cell lines were performed using the Seahorse XFp Cell Mito Stress Kit (Agilent Technologies) on the Seahorse XFe96 Analyzer. Cells were resuspended in

608 XF RPMI base media supplemented with 1 mM pyruvate, 2 mM L-glutamine, 10 mM glucose. 1 x
609 10^5 cells/well were seeded in poly-D-lysine (Thermofisher) coated XFe96 plates. The plate was
610 incubated in a non-CO_2 incubator at 37ºC for 1 hour to equilibrate. OCR and ECAR measurements
611 were taken at baseline and every 8 minutes after sequential addition of oligomycin (2 uM), FCCP
612 (0.5 uM), and rotenone/ antimycin A (0.75 uM). All measurements were normalized to the number
613 of viable cells.
614
615 **Generation of *PPM1D* WT U2OS cells using CRISPR editing**
616 U2OS cells containing the DR-GFP (for homologous recombination) or EJ5-GFP (for non-
617 homologous end-joining) DNA repair reporter cassettes were kindly provided by the Bertuch Lab
618 at Baylor College of Medicine. To establish *PPM1D*-WT isogenic lines, knock-in CRISPR editing
619 was performed with a single-stranded oligodeoxynucleotide (ssODN) template: TGCCCTGGTTC
620 GTAGCAATGCCTTCTCAGAGAATTTTCTAGAGGTTTCAGCTGAGATAGCTCGTGAGAATGT
621 ACAAGGTGTAGTCATACCCTAAAAGATCCAGAACCACTTGAAGAAAATGCGCTAAAGCCCT
622 GACTTTAAGGATACA. The *PPM1D* sgRNA sequence used was: ATAGCTCGAGA
623 GAATGTCCA. 1.3 ug of Cas9 (IDT) was incubated with 1 ug of sgRNA for 15 minutes at room
624 temperature. 1 ug of the ssODN template was then added to the Cas9-sgRNA complexes and
625 mixed with 20,000 U2OS cells and resuspended in 10 uL of Buffer R, immediately prior to
626 electroporation. The neon electroporation system was used with the following conditions: 1400v,
627 15 ms, 4 pulses. Single cell-derived clones were genotyped by Sanger sequencing and PPM1D
628 protein expression was validated by western blot.
629
630 **GFP reporter-based DNA repair assays**
631 For the DNA repair reporter assay, 100,000 U2OS cells were seeded in a 12-well plate in
632 antibiotic-free Dulbecco's Modified Eagle Medium (DMEM, Thermofisher) supplemented with 10%
633 FBS. Cells were transfected with 3.6 uL of Lipofectamine 2000 (Invitrogen) in 200 uL of OptiMEM
634 with 0.8 ug of the I-SceI expression plasmid (pCBASce, Addgene #6096*0*). The media was
635 replaced the next morning and the cells were trypsinized 48-hours post-transfection for analysis
636 of GFP expression by flow cytometry (BD Biosciences).
637
638 **Immunofluorescence microscopy**
639 12 mm glass coverslips were coated with 50 ug/mL poly-D-lysine (Thermofisher) for 30 minutes
640 at room temperature and washed with sterile PBS. 0.5 x 10^6 suspension cells/well were seeded
641 on coverslips and incubated for 1 hour at 37ºC to allow for adherence. Samples were then fixed
642 with 4% paraformaldehyde for 10 minutes at 37ºC and washed three times with 0.01% Triton-X
643 PBS (PBS-T). Fixed cells were permeabilized with 0.5% PBS-T for 20 minutes, washed three
644 times, and incubated with 5% goat serum (Thermofisher) for 1 hour at room temperature.
645 Afterwards, samples were incubated overnight at 4ºC with the following primary antibodies: rabbit
646 anti-Rad51 (Cell Signaling #8875S 1:100) or rabbit anti-53BP1 (ThermoFisher #PA1-16565,
647 1:500). The following day, samples were washed and incubated at room temperature for 1 hour
648 with Alexafluor 488-conjugated goat anti-rabbit IgG (#111-545-144, Jackson ImmunoResearch,
649 1:500). After secondary antibody incubation, the coverslips were washed three times with PBS
650 and mounted with fluoromount-G mounting medium with DAPI (Thermofisher) on glass

microscope slides and sealed with nail polish. Imaging was done on the Keyence BZ-X800 microscope and foci analysis was performed using CellProfiler.

Immunoblotting

Cells were lysed with 1x RIPA buffer supplemented with Halt Protease and Phosphatase inhibitor cocktail (Thermofischer) for 1 hour at 4ºC. Protein concentration was quantified using the Pierce BCA protein assay kit (Thermofischer) and boiled at 95ºC in 1x Laemmli (Biorad) for 7 minutes. The samples in which mitochondrial proteins were probed were not boiled, as boiling can cause signal reduction. Instead, samples were warmed to 37ºC for 30 minutes prior to loading. The proteins were separated by SDS-PAGE on 4-15% gradient gels (Biorad) and transferred on to PVDF membranes using the iBlot Dry Blotting system (Thermofisher). Membranes were incubated for 1 hour at room temperature in 5% milk in Tris-buffered saline solution with Tween-20 (TBST). After washing, the membranes were incubated overnight at 4ºC with the following primary antibodies: mouse anti-PPM1D (F-10, Santa Cruz, 1:1000), mouse anti-GAPDH (MAB374, Millipore, 1:200), mouse total OXPHOS Human antibody cocktail (ab110411, Abcam, 1:1000), mouse anti-Vinculin (V9131, Sigma Aldrich, 1:2000). The following day, membranes were washed twice with TBST and incubated for 1 hour with HRP-linked anti-rabbit IgG or anti-mouse IgG (Cell Signaling, 1:5000 – 1:10,000) at room temperature. Blots were imaged on the Bio-Rad ChemiDoc platform.

Statistical analysis

Statistical analysis incorporated in the MaGECK-VISPR algorithm includes p-value and FDR calculations. GraphPad Prism 6.0 was used for other statistical analyses. The sample size (n) specified in the Figure Legends was used for statistical analysis and denotes the number of independent biological replicates. The main conclusions were supported by data obtained from at least two biological replicates. The graphs presented in the figures are shown with error bars indicating either mean ± SEM or mean ± SD, as mentioned in the Figure Legends. Two-tailed t-tests were performed to calculate statistics, assuming unequal standard deviations, unless mentioned otherwise. Significance levels are indicated in the figures and were determined using GraphPad PRISM. Results were considered statistically significant at *$p<0.05$, **$p<0.01$, ***$p<0.001$, ****$p<0.0001$.

Acknowledgments

This work was supported by R01CA237291 and P01CA265748. This work was also supported by the NCI Cancer Center Support Grant P30CA125123 which partly supports the Cytometry Core, the Proteomics & Metabolomics Core, and the Antibody-based Proteomics Core. Support for the cores was also provided by the Cancer Prevention and Research Institute of Texas (CPRIT) from grants: RP180672, RR024574, and RP210227 and NIH S10OD028648. LZ was supported by the Baylor Research Advocates for Student Scientists (BRASS) Foundation, and the Janice McNair Medical Foundation.

Author Contributions:

Conceptualization: LZ, JIH, SMW, AT, AN, JNA, KT, GV, MAG
Methodology: LZ, JIH, EDB, CWC, AT, RM, RR, SJ, LV, BBadV
Investigation: LZ, JIH, EDB, CWC, AGG, AGM, SMW, EC, RM, RR, AN, SJ, SH, JNA
Visualization: LZ, EC, TJP, SMW
Computational analysis: EDB, CWC, TDP
Supervision: JIH, AN, BBAdV, CC, JNA, KT, GV, MAG
Writing—original draft: LZ, JIH
Writing—review & editing: LZ, JIH, EDB, GV, SMW, CWC, AT, MAG,
Contributed unpublished, essential data, or reagents: KT, HU, AGG, AGM, RM, RR, JNA

Competing Interests: The authors declare they have no competing interests.

Data and materials availability: All data are available in the main text or in the supplementary materials. All raw and processed data generated in this work will be publicly available at GEO data repositor pending scientific review. The human cell lines generated by the Goodell laboratory for this study are available upon request and will require a standard Materials Transfer Agreement (MTA). Any additional information required to analyze the data reported in this paper is available from the lead contact upon request.

References

1. Ali, A.Y., Abedini, M.R., and Tsang, B.K. (2012). The oncogenic phosphatase PPM1D confers cisplatin resistance in ovarian carcinoma cells by attenuating checkpoint kinase 1 and p53 activation. Oncogene *31*, 2175-2186.
2. Ardeljan, D., Steranka, J.P., Liu, C., Li, Z., Taylor, M.S., Payer, L.M., Gorbounov, M., Sarnecki, J.S., Deshpande, V., Hruban, R.H.*, et al.* (2020). Cell fitness screens reveal a conflict between LINE-1 retrotransposition and DNA replication. Nat Struct Mol Biol *27*, 168-178.
3. Bar, O., Ebenau, L., Weiner, K., Mintz, M., and Boles, R.G. (2023). Whole exome/genome sequencing in cyclic vomiting syndrome reveals multiple candidate genes, suggesting a model of elevated intracellular cations and mitochondrial dysfunction. Front Neurol *14*, 1151835.
4. Bolton, K.L., Ptashkin, R.N., Gao, T., Braunstein, L., Devlin, S.M., Kelly, D., Patel, M., Berthon, A., Syed, A., Yabe, M.*, et al.* (2020). Cancer therapy shapes the fitness landscape of clonal hematopoiesis. Nat Genet *52*, 1219-1226.
5. Bulavin, D.V., Demidov, O.N., Saito, S., Kauraniemi, P., Phillips, C., Amundson, S.A., Ambrosino, C., Sauter, G., Nebreda, A.R., Anderson, C.W.*, et al.* (2002). Amplification of PPM1D in human tumors abrogates p53 tumor-suppressor activity. Nat Genet *31*, 210-215.
6. Burdova, K., Storchova, R., Palek, M., and Macurek, L. (2019). WIP1 Promotes Homologous Recombination and Modulates Sensitivity to PARP Inhibitors. Cells *8*.
7. Ceccaldi, R., Sarangi, P., and D'Andrea, A.D. (2016). The Fanconi anaemia pathway: new players and new functions. Nat Rev Mol Cell Biol *17*, 337-349.
8. Cha, H., Lowe, J.M., Li, H., Lee, J.S., Belova, G.I., Bulavin, D.V., and Fornace, A.J., Jr. (2010). Wip1 directly dephosphorylates gamma-H2AX and attenuates the DNA damage response. Cancer Res *70*, 4112-4122.
9. Ciccia, A., and Elledge, S.J. (2010). The DNA damage response: making it safe to play with knives. Mol Cell *40*, 179-204.
10. Coarfa, C., Grimm, S.L., Rajapakshe, K., Perera, D., Lu, H.Y., Wang, X., Christensen, K.R., Mo, Q., Edwards, D.P., and Huang, S. (2021). Reverse-Phase Protein Array: Technology, Application, Data Processing, and Integration. J Biomol Tech.
11. Dhar, S.K., Tangpong, J., Chaiswing, L., Oberley, T.D., and St Clair, D.K. (2011). Manganese superoxide dismutase is a p53-regulated gene that switches cancers between early and advanced stages. Cancer Res *71*, 6684-6695.
12. Dobin, A., Davis, C.A., Schlesinger, F., Drenkow, J., Zaleski, C., Jha, S., Batut, P., Chaisson, M., and Gingeras, T.R. (2013). STAR: ultrafast universal RNA-seq aligner. Bioinformatics *29*, 15-21.
13. Feng, X., Tang, M., Dede, M., Su, D., Pei, G., Jiang, D., Wang, C., Chen, Z., Li, M., Nie, L.*, et al.* (2022). Genome-wide CRISPR screens using isogenic cells reveal vulnerabilities conferred by loss of tumor suppressors. Sci Adv *8*, eabm6638.
14. Fiscella, M., Zhang, H., Fan, S., Sakaguchi, K., Shen, S., Mercer, W.E., Vande Woude, G.F., O'Connor, P.M., and Appella, E. (1997). Wip1, a novel human protein phosphatase that is induced in response to ionizing radiation in a p53-dependent manner. Proc Natl Acad Sci U S A *94*, 6048-6053.
15. Fu, Z., Sun, G., and Gu, T. (2014). Proto-oncogene Wip1, a member of a new family of proliferative genes in NSCLC and its clinical significance. Tumour Biol *35*, 2975-2981.
16. Genovese, G., Kahler, A.K., Handsaker, R.E., Lindberg, J., Rose, S.A., Bakhoum, S.F., Chambert, K., Mick, E., Neale, B.M., Fromer, M.*, et al.* (2014). Clonal hematopoiesis and blood-cancer risk inferred from blood DNA sequence. N Engl J Med *371*, 2477-2487.
17. Greve, B., Bolling, T., Amler, S., Rossler, U., Gomolka, M., Mayer, C., Popanda, O., Dreffke, K., Rickinger, A., Fritz, E.*, et al.* (2012). Evaluation of different biomarkers to predict

759 individual radiosensitivity in an inter-laboratory comparison--lessons for future studies. PLoS
760 One *7*, e47185.
761 18. Guleria, A., and Chandna, S. (2016). ATM kinase: Much more than a DNA damage
762 responsive protein. DNA Repair (Amst) *39*, 1-20.
763 19. Hanahan, D., and Weinberg, R.A. (2011). Hallmarks of cancer: the next generation. Cell
764 *144*, 646-674.
765 20. Harper, J.W., Adami, G.R., Wei, N., Keyomarsi, K., and Elledge, S.J. (1993). The p21 Cdk-
766 interacting protein Cip1 is a potent inhibitor of G1 cyclin-dependent kinases. Cell *75*, 805-
767 816.
768 21. Hawash, M., Jaradat, N., Abualhasan, M., Thaher, M., Sawalhi, R., Younes, N., Shanaa, A.,
769 Nuseirat, M., and Mousa, A. (2022). In vitro and in vivo assessment of the antioxidant
770 potential of isoxazole derivatives. Sci Rep *12*, 18223.
771 22. He, X.L., Xiao, Q., Zhou, Z.P., and Hui, C.Y. (2021). PPM1D accelerates proliferation and
772 metastasis of osteosarcoma by activating PKP2. Eur Rev Med Pharmacol Sci *25*, 78-85.
773 23. Hoeijmakers, J.H. (2009). DNA damage, aging, and cancer. N Engl J Med *361*, 1475-1485.
774 24. Hsu, J.I., Dayaram, T., Tovy, A., De Braekeleer, E., Jeong, M., Wang, F., Zhang, J.,
775 Heffernan, T.P., Gera, S., Kovacs, J.J.*, et al.* (2018). PPM1D Mutations Drive Clonal
776 Hematopoiesis in Response to Cytotoxic Chemotherapy. Cell Stem Cell *23*, 700-713 e706.
777 25. Jaiswal, S., Fontanillas, P., Flannick, J., Manning, A., Grauman, P.V., Mar, B.G., Lindsley,
778 R.C., Mermel, C.H., Burtt, N., Chavez, A.*, et al.* (2014). Age-related clonal hematopoiesis
779 associated with adverse outcomes. N Engl J Med *371*, 2488-2498.
780 26. Jansen, S., Geuer, S., Pfundt, R., Brough, R., Ghongane, P., Herkert, J.C., Marco, E.J.,
781 Willemsen, M.H., Kleefstra, T., Hannibal, M.*, et al.* (2017). De Novo Truncating Mutations in
782 the Last and Penultimate Exons of PPM1D Cause an Intellectual Disability Syndrome. Am
783 J Hum Genet *100*, 650-658.
784 27. Jiao, L., Shen, D., Liu, G., Jia, J., Geng, J., Wang, H., and Sun, Y. (2014). PPM1D as a
785 novel biomarker for prostate cancer after radical prostatectomy. Anticancer Res *34*, 2919-
786 2925.
787 28. Juarez, J.C., Betancourt, O., Jr., Pirie-Shepherd, S.R., Guan, X., Price, M.L., Shaw, D.E.,
788 Mazar, A.P., and Donate, F. (2006). Copper binding by tetrathiomolybdate attenuates
789 angiogenesis and tumor cell proliferation through the inhibition of superoxide dismutase 1.
790 Clin Cancer Res *12*, 4974-4982.
791 29. Kahn, J.D., Miller, P.G., Silver, A.J., Sellar, R.S., Bhatt, S., Gibson, C., McConkey, M.,
792 Adams, D., Mar, B., Mertins, P.*, et al.* (2018). PPM1D-truncating mutations confer resistance
793 to chemotherapy and sensitivity to PPM1D inhibition in hematopoietic cells. Blood *132*,
794 1095-1105.
795 30. Kang, M.Y., Kim, H.B., Piao, C., Lee, K.H., Hyun, J.W., Chang, I.Y., and You, H.J. (2013).
796 The critical role of catalase in prooxidant and antioxidant function of p53. Cell Death Differ
797 *20*, 117-129.
798 31. Khadka, P., Reitman, Z.J., Lu, S., Buchan, G., Gionet, G., Dubois, F., Carvalho, D.M., Shih,
799 J., Zhang, S., Greenwald, N.F.*, et al.* (2022). PPM1D mutations are oncogenic drivers of de
800 novo diffuse midline glioma formation. Nat Commun *13*, 604.
801 32. Kottemann, M.C., and Smogorzewska, A. (2013). Fanconi anaemia and the repair of
802 Watson and Crick DNA crosslinks. Nature *493*, 356-363.
803 33. Lambros, M.B., Natrajan, R., Geyer, F.C., Lopez-Garcia, M.A., Dedes, K.J., Savage, K.,
804 Lacroix-Triki, M., Jones, R.L., Lord, C.J., Linardopoulos, S.*, et al.* (2010). PPM1D gene
805 amplification and overexpression in breast cancer: a qRT-PCR and chromogenic in situ
806 hybridization study. Mod Pathol *23*, 1334-1345.
807 34. Li, B., Hu, J., He, D., Chen, Q., Liu, S., Zhu, X., and Yu, M. (2020a). PPM1D Knockdown
808 Suppresses Cell Proliferation, Promotes Cell Apoptosis, and Activates p38 MAPK/p53

Signaling Pathway in Acute Myeloid Leukemia. Technol Cancer Res Treat *19*, 1533033820942312.

35. Li, J., Yang, Y., Peng, Y., Austin, R.J., van Eyndhoven, W.G., Nguyen, K.C., Gabriele, T., McCurrach, M.E., Marks, J.R., Hoey, T.*, et al.* (2002). Oncogenic properties of PPM1D located within a breast cancer amplification epicenter at 17q23. Nat Genet *31*, 133-134.
36. Li, K., Liu, Y., Xu, S., and Wang, J. (2020b). PPM1D Functions as Oncogene and is Associated with Poor Prognosis in Esophageal Squamous Cell Carcinoma. Pathol Oncol Res *26*, 387-395.
37. Li, W., Xu, H., Xiao, T., Cong, L., Love, M.I., Zhang, F., Irizarry, R.A., Liu, J.S., Brown, M., and Liu, X.S. (2014). MAGeCK enables robust identification of essential genes from genome-scale CRISPR/Cas9 knockout screens. Genome Biol *15*, 554.
38. Liang, Y., Liu, J., and Feng, Z. (2013). The regulation of cellular metabolism by tumor suppressor p53. Cell Biosci *3*, 9.
39. Liao, Y., Smyth, G.K., and Shi, W. (2014). featureCounts: an efficient general purpose program for assigning sequence reads to genomic features. Bioinformatics *30*, 923-930.
40. Lin, J., Zahurak, M., Beer, T.M., Ryan, C.J., Wilding, G., Mathew, P., Morris, M., Callahan, J.A., Gordon, G., Reich, S.D.*, et al.* (2013). A non-comparative randomized phase II study of 2 doses of ATN-224, a copper/zinc superoxide dismutase inhibitor, in patients with biochemically recurrent hormone-naive prostate cancer. Urol Oncol *31*, 581-588.
41. Lindsley, R.C., Saber, W., Mar, B.G., Redd, R., Wang, T., Haagenson, M.D., Grauman, P.V., Hu, Z.H., Spellman, S.R., Lee, S.J.*, et al.* (2017). Prognostic Mutations in Myelodysplastic Syndrome after Stem-Cell Transplantation. N Engl J Med *376*, 536-547.
42. Ling, M., Liu, Q., Wang, Y., Liu, X., Jiang, M., and Hu, J. (2022). LCS-1 inhibition of superoxide dismutase 1 induces ROS-dependent death of glioma cells and degradates PARP and BRCA1. Front Oncol *12*, 937444.
43. Love, M.I., Huber, W., and Anders, S. (2014). Moderated estimation of fold change and dispersion for RNA-seq data with DESeq2. Genome Biol *15*, 550.
44. Lowndes, S.A., Adams, A., Timms, A., Fisher, N., Smythe, J., Watt, S.M., Joel, S., Donate, F., Hayward, C., Reich, S.*, et al.* (2008). Phase I study of copper-binding agent ATN-224 in patients with advanced solid tumors. Clin Cancer Res *14*, 7526-7534.
45. Lu H.-Y., X.J., Perera D.N., Rajapakshe K., Wang X., Costello M., Holloway K.R., Ramos C., Grimm S.L., Julia Wulfkuhle, Coarfa C, Edwards D.P., Zhu M.X., Huang S. (2021). High-Throughput Evaluation of Metabolic Activities Using Reverse Phase Protein Array Technology. In Neuron Signaling in Metabolic Regulation (Boca Raton: CRC Press), p. 25.
46. Lu, X., Nannenga, B., and Donehower, L.A. (2005). PPM1D dephosphorylates Chk1 and p53 and abrogates cell cycle checkpoints. Genes Dev *19*, 1162-1174.
47. Maya-Mendoza, A., Ostrakova, J., Kosar, M., Hall, A., Duskova, P., Mistrik, M., Merchut-Maya, J.M., Hodny, Z., Bartkova, J., Christensen, C.*, et al.* (2015). Myc and Ras oncogenes engage different energy metabolism programs and evoke distinct patterns of oxidative and DNA replication stress. Mol Oncol *9*, 601-616.
48. Miller, P.G., Sathappa, M., Moroco, J.A., Jiang, W., Qian, Y., Iqbal, S., Guo, Q., Giacomelli, A.O., Shaw, S., Vernier, C.*, et al.* (2022). Allosteric inhibition of PPM1D serine/threonine phosphatase via an altered conformational state. Nat Commun *13*, 3778.
49. Nguyen, T.A., Slattery, S.D., Moon, S.H., Darlington, Y.F., Lu, X., and Donehower, L.A. (2010). The oncogenic phosphatase WIP1 negatively regulates nucleotide excision repair. DNA Repair (Amst) *9*, 813-823.
50. Oliva-Trastoy, M., Berthonaud, V., Chevalier, A., Ducrot, C., Marsolier-Kergoat, M.C., Mann, C., and Leteurtre, F. (2007). The Wip1 phosphatase (PPM1D) antagonizes activation of the Chk2 tumour suppressor kinase. Oncogene *26*, 1449-1458.

858 51. Park, M.T., Kim, M.J., Suh, Y., Kim, R.K., Kim, H., Lim, E.J., Yoo, K.C., Lee, G.H., Kim, Y.H.,
859 Hwang, S.G., *et al.* (2014). Novel signaling axis for ROS generation during K-Ras-induced
860 cellular transformation. Cell Death Differ *21*, 1185-1197.
861 52. Peng, B., Wang, J., Hu, Y., Zhao, H., Hou, W., Zhao, H., Wang, H., Liao, J., and Xu, X.
862 (2015). Modulation of LSD1 phosphorylation by CK2/WIP1 regulates RNF168-dependent
863 53BP1 recruitment in response to DNA damage. Nucleic Acids Res *43*, 5936-5947.
864 53. Peng, T.S., He, Y.H., Nie, T., Hu, X.D., Lu, H.Y., Yi, J., Shuai, Y.F., and Luo, M. (2014).
865 PPM1D is a prognostic marker and therapeutic target in colorectal cancer. Exp Ther Med *8*,
866 430-434.
867 54. Peuget, S., Bonacci, T., Soubeyran, P., Iovanna, J., and Dusetti, N.J. (2014). Oxidative
868 stress-induced p53 activity is enhanced by a redox-sensitive TP53INP1 SUMOylation. Cell
869 Death Differ *21*, 1107-1118.
870 55. Ruark, E., Snape, K., Humburg, P., Loveday, C., Bajrami, I., Brough, R., Rodrigues, D.N.,
871 Renwick, A., Seal, S., Ramsay, E., *et al.* (2013). Mosaic PPM1D mutations are associated
872 with predisposition to breast and ovarian cancer. Nature *493*, 406-410.
873 56. Sablina, A.A., Budanov, A.V., Ilyinskaya, G.V., Agapova, L.S., Kravchenko, J.E., and
874 Chumakov, P.M. (2005). The antioxidant function of the p53 tumor suppressor. Nat Med *11*,
875 1306-1313.
876 57. Sajesh, B.V., Bailey, M., Lichtensztejn, Z., Hieter, P., and McManus, K.J. (2013). Synthetic
877 lethal targeting of superoxide dismutase 1 selectively kills RAD54B-deficient colorectal
878 cancer cells. Genetics *195*, 757-767.
879 58. Sajesh, B.V., and McManus, K.J. (2015). Targeting SOD1 induces synthetic lethal killing in
880 BLM- and CHEK2-deficient colorectal cancer cells. Oncotarget *6*, 27907-27922.
881 59. Schlacher, K., Wu, H., and Jasin, M. (2012). A distinct replication fork protection pathway
882 connects Fanconi anemia tumor suppressors to RAD51-BRCA1/2. Cancer Cell *22*, 106-116.
883 60. Schmezer, P., Rajaee-Behbahani, N., Risch, A., Thiel, S., Rittgen, W., Drings, P.,
884 Dienemann, H., Kayser, K.W., Schulz, V., and Bartsch, H. (2001). Rapid screening assay
885 for mutagen sensitivity and DNA repair capacity in human peripheral blood lymphocytes.
886 Mutagenesis *16*, 25-30.
887 61. Somwar, R., Erdjument-Bromage, H., Larsson, E., Shum, D., Lockwood, W.W., Yang, G.,
888 Sander, C., Ouerfelli, O., Tempst, P.J., Djaballah, H., *et al.* (2011). Superoxide dismutase 1
889 (SOD1) is a target for a small molecule identified in a screen for inhibitors of the growth of
890 lung adenocarcinoma cell lines. Proc Natl Acad Sci U S A *108*, 16375-16380.
891 62. Takekawa, M., Adachi, M., Nakahata, A., Nakayama, I., Itoh, F., Tsukuda, H., Taya, Y., and
892 Imai, K. (2000). p53-inducible wip1 phosphatase mediates a negative feedback regulation
893 of p38 MAPK-p53 signaling in response to UV radiation. EMBO J *19*, 6517-6526.
894 63. Tan, M., Li, S., Swaroop, M., Guan, K., Oberley, L.W., and Sun, Y. (1999). Transcriptional
895 activation of the human glutathione peroxidase promoter by p53. J Biol Chem *274*, 12061-
896 12066.
897 64. Tokheim, C., Wang, X., Timms, R.T., Zhang, B., Mena, E.L., Wang, B., Chen, C., Ge, J.,
898 Chu, J., Zhang, W., *et al.* (2021). Systematic characterization of mutations altering protein
899 degradation in human cancers. Mol Cell *81*, 1292-1308 e1211.
900 65. Turrens, J.F. (2003). Mitochondrial formation of reactive oxygen species. Journal of
901 Physiology *552*, 335-344.
902 66. Tzelepis, K., Koike-Yusa, H., De Braekeleer, E., Li, Y., Metzakopian, E., Dovey, O.M., Mupo,
903 A., Grinkevich, V., Li, M., Mazan, M., *et al.* (2016). A CRISPR Dropout Screen Identifies
904 Genetic Vulnerabilities and Therapeutic Targets in Acute Myeloid Leukemia. Cell Rep *17*,
905 1193-1205.
906 67. Wallace, D.C. (2005). A mitochondrial paradigm of metabolic and degenerative diseases,
907 aging, and cancer: a dawn for evolutionary medicine. Annu Rev Genet *39*, 359-407.

68. Wang, P., Rao, J., Yang, H., Zhao, H., and Yang, L. (2011). PPM1D silencing by lentiviral-mediated RNA interference inhibits proliferation and invasion of human glioma cells. J Huazhong Univ Sci Technolog Med Sci *31*, 94-99.
69. Wang, X., Shi, Z., Lu, H.Y., Kim, J.J., Bu, W., Villalobos, J.A., Perera, D.N., Jung, S.Y., Wang, T., Grimm, S.L.*, et al.* (2022). High-throughput profiling of histone post-translational modifications and chromatin modifying proteins by reverse phase protein array. J Proteomics *262*, 104596.
70. Weinstock, D.M., Nakanishi, K., Helgadottir, H.R., and Jasin, M. (2006). Assaying double-strand break repair pathway choice in mammalian cells using a targeted endonuclease or the RAG recombinase. Methods Enzymol *409*, 524-540.
71. Wojcik, M.H., Srivastava, S., Agrawal, P.B., Balci, T.B., Callewaert, B., Calvo, P.L., Carli, D., Caudle, M., Colaiacovo, S., Cross, L.*, et al.* (2023). Jansen-de Vries syndrome: Expansion of the PPM1D clinical and phenotypic spectrum in 34 families. Am J Med Genet A.
72. Wu, B., Guo, B.M., Kang, J., Deng, X.Z., Fan, Y.B., Zhang, X.P., and Ai, K.X. (2016). PPM1D exerts its oncogenic properties in human pancreatic cancer through multiple mechanisms. Apoptosis *21*, 365-378.
73. Yin, H., Yan, Z., Liang, Y., Liu, B., and Su, Q. (2013). Knockdown of protein phosphatase magnesium-dependent 1 (PPM1D) through lentivirus-mediated RNA silencing inhibits colorectal carcinoma cell proliferation. Technol Cancer Res Treat *12*, 537-543.
74. Yokoyama, A., Kakiuchi, N., Yoshizato, T., Nannya, Y., Suzuki, H., Takeuchi, Y., Shiozawa, Y., Sato, Y., Aoki, K., Kim, S.K.*, et al.* (2019). Age-related remodelling of oesophageal epithelia by mutated cancer drivers. Nature *565*, 312-317.
75. Yonish-Rouach, E., Resnitzky, D., Lotem, J., Sachs, L., Kimchi, A., and Oren, M. (1991). Wild-type p53 induces apoptosis of myeloid leukaemic cells that is inhibited by interleukin-6. Nature *352*, 345-347.
76. Zhang, L., Chen, L.H., Wan, H., Yang, R., Wang, Z., Feng, J., Yang, S., Jones, S., Wang, S., Zhou, W.*, et al.* (2014). Exome sequencing identifies somatic gain-of-function PPM1D mutations in brainstem gliomas. Nat Genet *46*, 726-730.
77. Zong, D., Adam, S., Wang, Y., Sasanuma, H., Callen, E., Murga, M., Day, A., Kruhlak, M.J., Wong, N., Munro, M.*, et al.* (2019). BRCA1 Haploinsufficiency Is Masked by RNF168-Mediated Chromatin Ubiquitylation. Mol Cell *73*, 1267-1281 e1267.

Figure 1

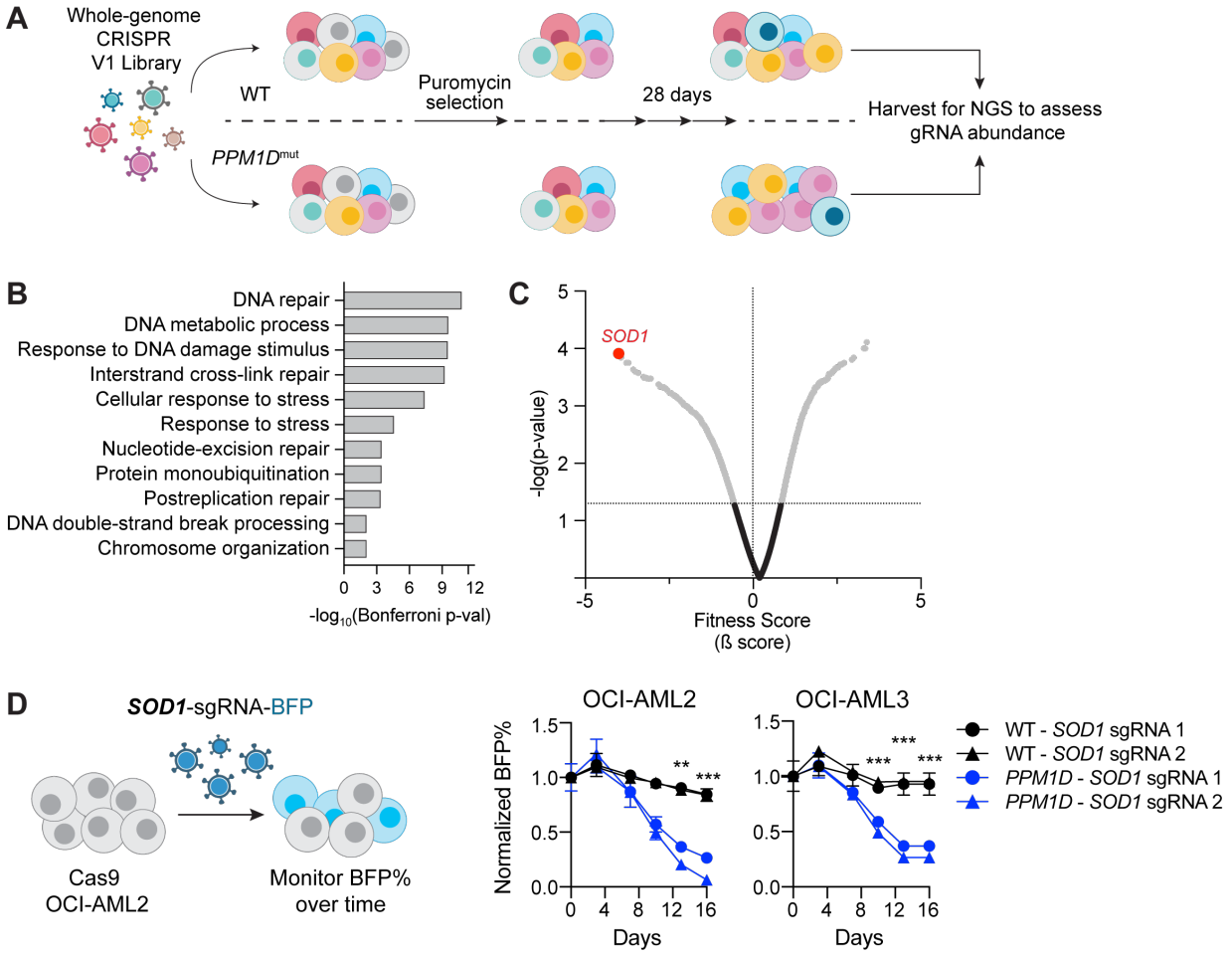

Figure 1. *SOD1* is a synthetic lethal vulnerability of *PPM1D*-mutant leukemia cells. (A) Schematic of whole-genome CRISPR dropout screen. WT Cas9-expressing OCI-AML2 and two isogenic *PPM1D*-mutant lines with three technical replicates were transduced with the Human Improved Whole Genome Knockout CRISPR library V1 containing 90,709 guide RNAs (gRNAs) targeting 18,010 human genes at low multiplicity of infection (MOI~0.3). Three days post-transduction, cells underwent puromycin selection for three days. Cells were harvested at day 10 as the initial timepoint and then harvested every three days. sgRNA sequencing was performed on cells collected on day 28. **(B)** Top biological processes based on gene ontology analysis of the top 37 genes essential for *PPM1D*-mutant cell survival. Enrichment and depletion of guides and genes were analyzed using MAGeCK-VISPR by comparing read counts from each *PPM1D*-mutant cell line replicate with counts from the initial starting population at day ten. **(C)** Volcano plot of synthetic lethal hits ranked by fitness score with a negative score indicating genes for which their knockout leads decreased growth or survival. *SOD1* (highlighted) was the top hit from the screen. **(D)** Left: Schematic of competitive proliferation assays used for validation of CRISPR targets. Right: WT and *PPM1D*-mutant Cas9-OCI-AML2 and Cas9-OCI-AML3 cells were transduced with lentivirus containing a single *SOD1*-gRNA with a blue fluorescent protein (BFP) reporter. Cells were assayed by flow cytometry every 3-4 days post-transduction and normalized to the BFP percentage at day 3. Two unique gRNAs against *SOD1* were used per cell line and each condition was performed in technical duplicates; multiple unpaired t-tests, **p<0.01, ***p<0.001.

Figure 2

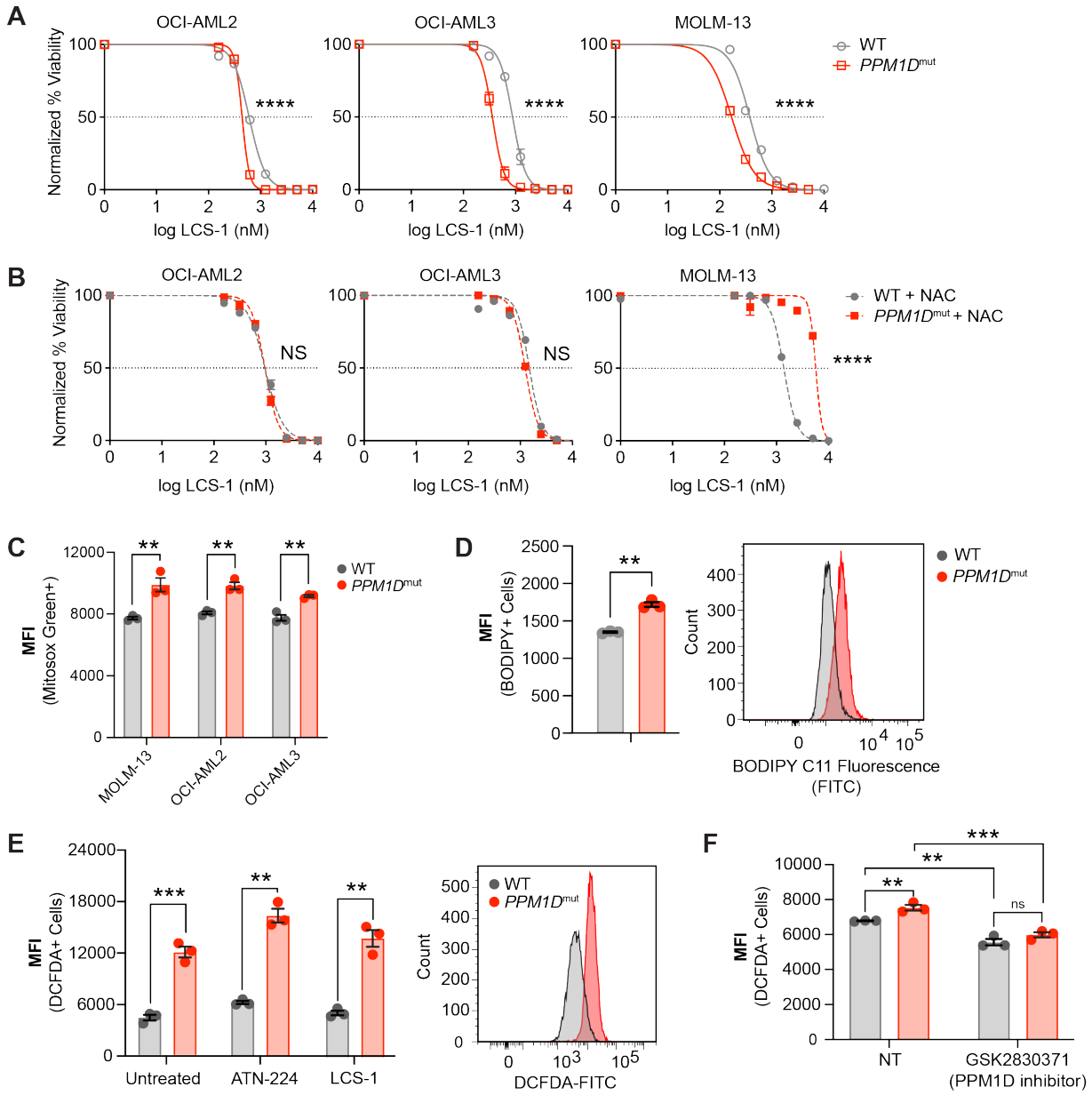
A
OCI-AML2
OCI-AML3
MOLM-13
Normalized % Viability
log LCS-1 (nM)
****
WT
PPM1Dmut
B
NS
WT + NAC
PPM1Dmut + NAC
C
MFI
(Mitosox Green+)
MOLM-13
OCI-AML2
OCI-AML3
D
MFI
(BODIPY+ Cells)
Count
BODIPY C11 Fluorescence
(FITC)
E
MFI
(DCFDA+ Cells)
Untreated
ATN-224
LCS-1
DCFDA-FITC
F
ns
NT
GSK2830371
(PPM1D inhibitor)

959

960 **Figure 2. *PPM1D*-mutant cells are sensitive to SOD1 inhibition and have increased oxidative stress.**
961 **(A,B)** Dose response curves for cell viability with SOD1-inhibitor (LCS-1) **(A)** or LCS-1 in combination with
962 0.25 uM NAC **(B)** in WT and *PPM1D*-mutant leukemia cell lines after 24-hours. Mean ± SD (n=3) is shown
963 with a non-linear regression curve. All values are normalized to the baseline cell viability with vehicle, as
964 measured by MTT assay. **(C)** Endogenous mitochondrial superoxide levels of WT and *PPM1D*-mutant
965 leukemia cell lines were measured using MitoSox Green staining (1 uM). The mean fluorescence intensity
966 (MFI) of MitoSox Green was measured by flow cytometry. Mean ± SD (n=3) is shown. **(D)** Lipid peroxidation
967 measured using BODIPY 581/591 staining (2.5 uM) of WT and *PPM1D*-mutant OCI-AML2 cells. The MFI
968 was measured by flow cytometry. Mean ± SD (n=3) is shown. **(E-F)** Measure of total reactive oxygen
969 species using 2',7'–dichlorofluorescin diacetate (DCFDA) staining (10 uM) measured by flow cytometry.
970 WT and *PPM1D*-mutant OCI-AML2 cells were measured at baseline and 24-hrs after SOD1 inhibition (ATN-
971 224 12.5 uM, LCS-1 0.625 uM) **(E)** or 24-hrs after pharmacologic PPM1D inhibition (GSK2830371, 5 uM)
972 **(F)**; unpaired t-tests were used for statistical analyses, ns=non-significant ($p>0.05$), **$p<0.01$, ***$p<0.001$,
973 ****$p<0.0001$.

Figure 3

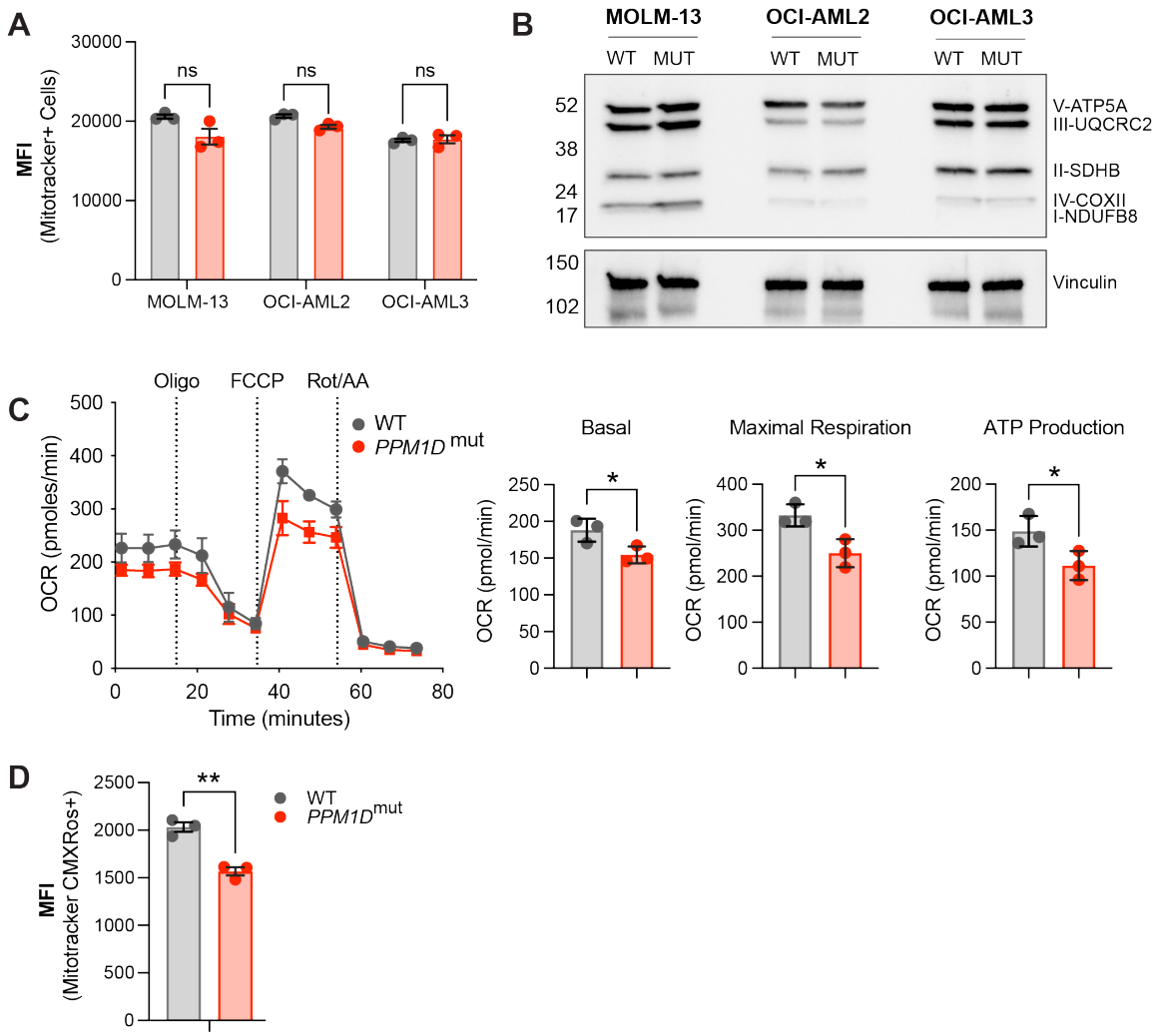

Figure 3. *PPM1D*-mutant cells have altered mitochondrial function. (A) Mitochondrial mass of WT and *PPM1D*-mutant leukemia cells was determined using MitoTracker Green (100 nM) and analzyed by flow cytometry. Data represents mean ± SD of triplicates. At least three independent experiments were conducted with similar findings; unpaired t-tests. **(B)** Immunoblot of WT and *PPM1D*-mutant cell lysates probed with the human OXPHOS antibody cocktail (1:1000) and vinculin (1:2000). **(C)** Measurement of mitochondrial oxygen consumption ratio (OCR) by seahorse assay in WT vs. *PPM1D*-mutant OCI-AML2 cells after treatment with oligomycin (1.5 uM), FCCP (0.5 uM), and rot/AA (0.5 uM). Quantification of basal, maximal, and ATP-linked respiration are shown. Data shown are the mean ± SD of technical triplicates. **(D)** Mitochondrial membrane potential of WT and *PPM1D*-mutant OCI-AML2 cells was measured using MitoTracker CMXRos (400 nM) and analyzed by flow cytometry. Data represents mean ± SD of triplicates, unpaired t-test, ns=non-significant ($p>0.05$), *$p<0.05$, **$p<0.01$.

Figure 4

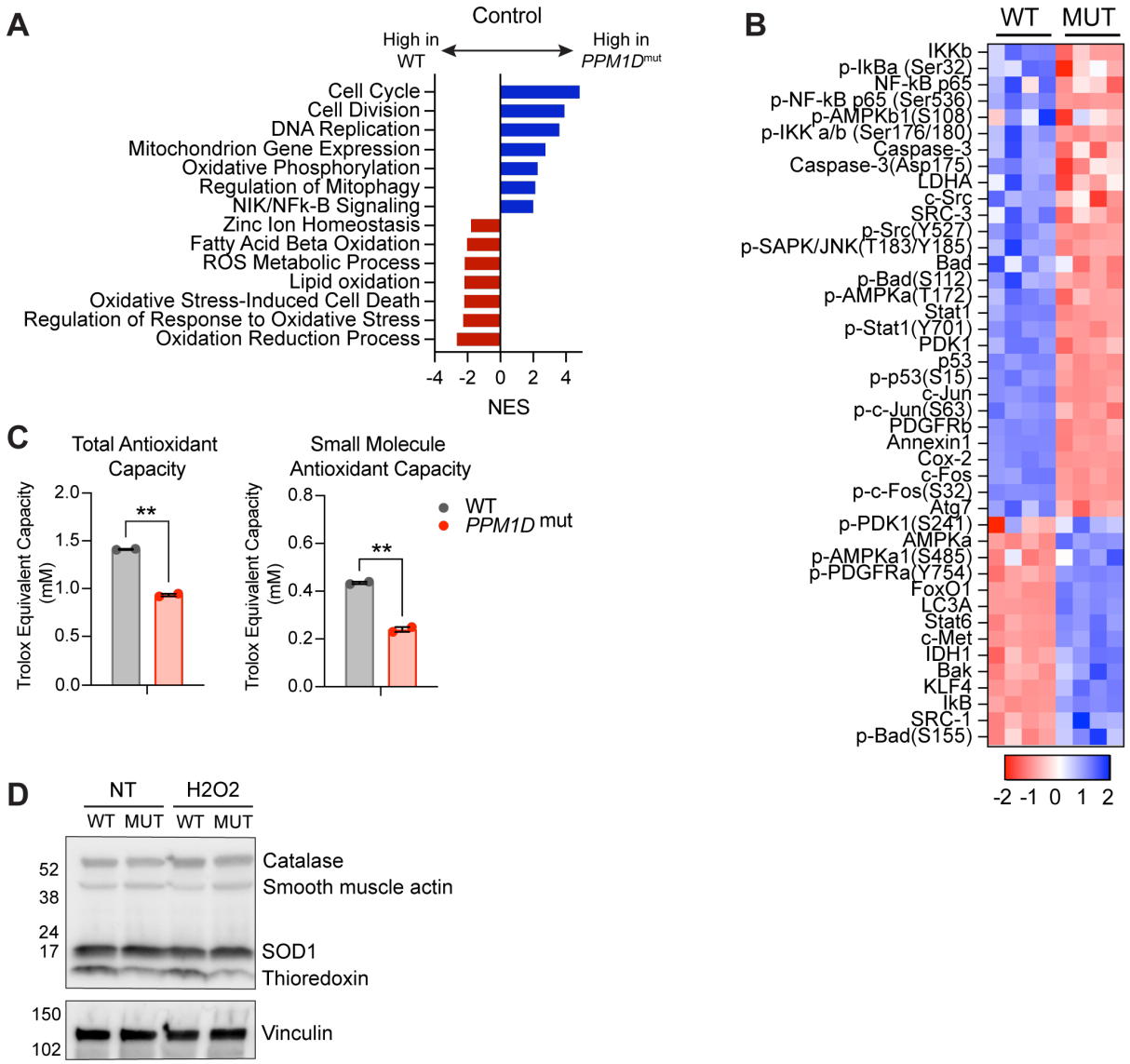

Figure 4. *PPM1D*-mutant cells have a reduced oxidative stress response. (A) RNA-seq GSEA analysis of *PPM1D*-mutant cells compared to WT Cas9-OCI-AML2 cells. Significantly up- and downregulated pathways are indicated by the blue and red bars, respectively. Normalized enrichment scores (NES) are shown with FDR <0.25. **(B)** RPPA profiling of WT and *PPM1D*-mutant OCI-AML2 cells. Proteins from the "Response to Oxidative Stress" pathway have been selected for the heatmap. Each column represents a technical replicate. See Figure 4-source data 2 for the raw data. **(C)** Total- and small molecule antioxidant capacity of WT and *PPM1D*-mutant cells performed in technical duplicates. Student t-test was used for statistical analysis, **p<0.01. **(D)** Immunoblot of WT and *PPM1D*-mutant OCI-AML2 cells in the untreated state (NT) or treated for 30 minutes with H2O2 (25 mM). Lysates were probed with an anti-oxidative stress defense cocktail (1:250) and vinculin (1:2000).

Figure 5

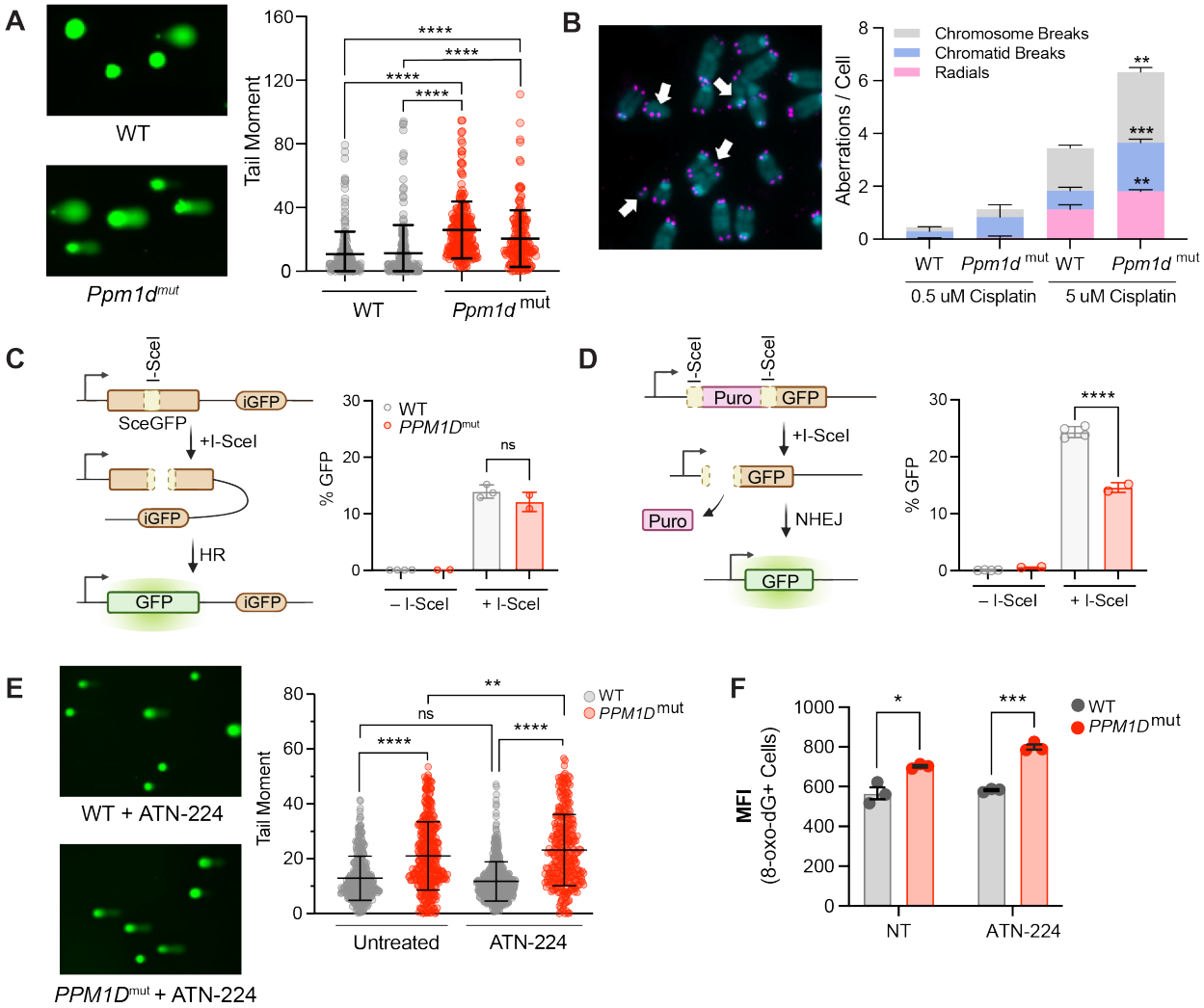

Figure 5. *PPM1D* mutations increase genomic instability and impair non-homologous end-joining. **(A)** Left: Representative images of comet assays of mouse embryonic fibroblasts (MEFs). Two biological replicates were assessed for each genotype. Right: Quantification of n≥150 comets per experimental group with the Comet IV software; 2way ANOVA. **(B)** Left: Representative images of metaphase spreads of WT and *Ppm1d*-mutant mouse primary B-cells treated with low (0.5 uM) or high (5 uM) doses of cisplatin. Right: n≥50 metaphase cells were quantified in each experimental condition for chromosomal aberrations (white arrows). n=2 biological replicates used for each genotype. Student's t-test was used for statistical analysis. **(C–D)** Left: Schematic of the homologous recombination **(C)** or non-homologous end-joining **(D)** U2OS DNA damage repair cassettes. Right: Quantification of GFP% analyzed by flow cytometry 48-hours after induction of DNA damage by I-SceI transduction; student's t-test. **(E)** Left: Representative images of comet assays of OCI-AML2 cells at baseline and treated with ATN-224 (12.5 uM) for 24 hours. Right: Quantification of n>150 comets per experimental group using the Comet IV software; 2way ANOVA. **(F)** MFI of 8-oxo-dG lesions within OCI-AML2 cells 48-hours after ATN-224 (12.5 uM) treatment compared to control (NT) as measured by flow cytometry. Data are mean ± SD (n=3), ns=non-significant (p>0.05), *p<0.05, **p<0.01, ***p<0.001, ****p<0.0001.

Figure 1 – Figure Supplement 1

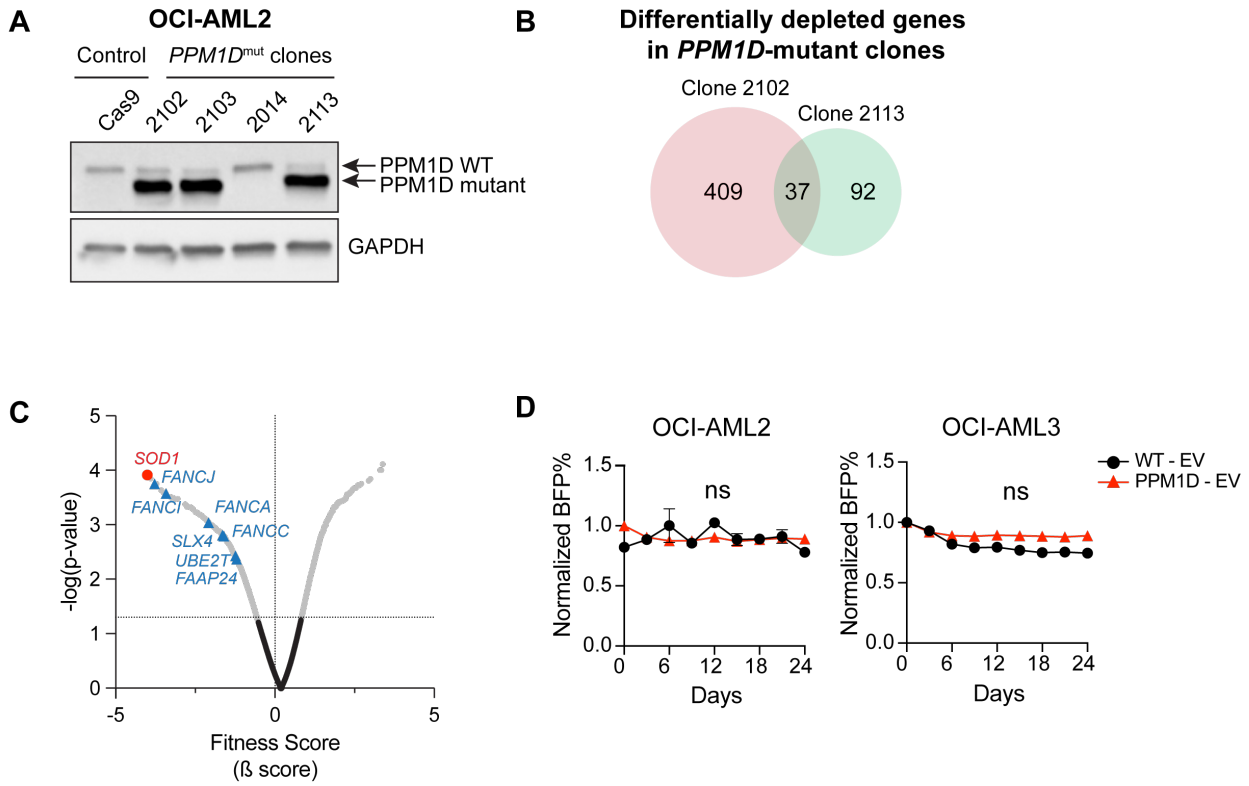

Figure 1 – Figure Supplement 1. Genome-wide CRISPR screen identifies *SOD1* as a synthetic lethal partner of *PPM1D*-mutant leukemia cells. (A) Immunoblot validation of *PPM1D*-mutant Cas9-expressing OCI-AML2 cells generated and used for CRISPR screening. Blots were probed with anti-PPM1D (1:1000) and GAPDH (1:1000). Clones 2102 and 2113 were selected for the dropout screen. **(B)** Venn diagram of genes that were depleted from the two *PPM1D*-mutant clones (#2102, 2113) used in the dropout screen, but not depleted in the WT control lines. 37 genes were found to be depleted in both mutant clones. For a full list of genes, see Figure 1-source data 1. **(C)** Volcano plot of synthetic lethal hits ranked by fitness score with the Fanconi Anemia pathway genes highlighted in blue. **(D)** Cas9-OCI-AML2 and Cas9-OCI-AML3 WT or *PPM1D*-mutant cells were transduced with the empty vector control backbone tagged with a blue fluorescent protein (BFP) reporter. Cells were assayed by flow cytometry between 3- and 24-days post-transduction and normalized to the BFP percentage at day 3. Data shown are mean ± SD (n=2 per condition).

Figure 2 – Figure Supplement 1

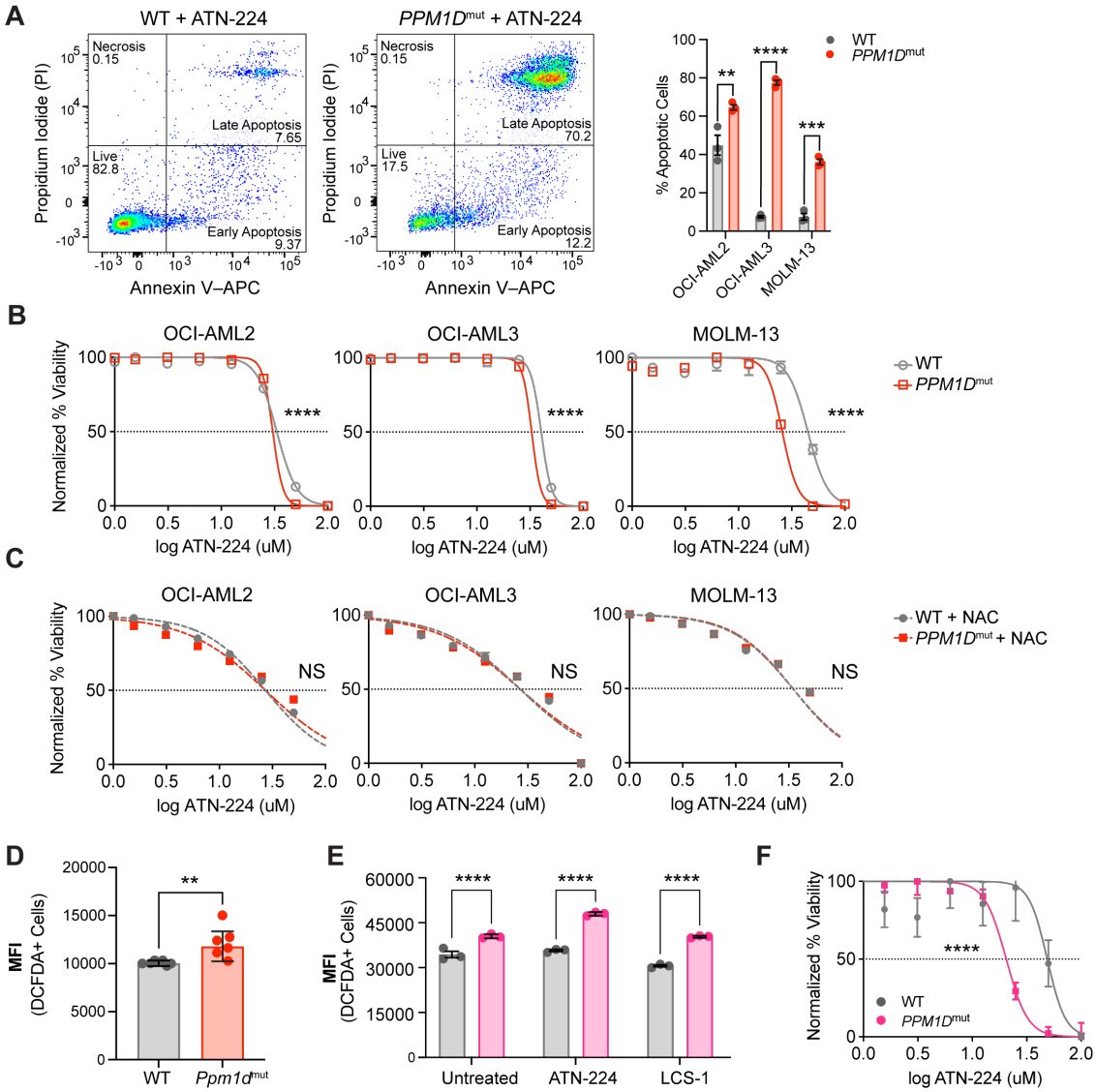

Figure 2 – Figure Supplement 1. *PPM1D*-mutant cells have increased oxidative stress. (A) Left: Representative flow cytometry plots of WT and *PPM1D*-mutant cells treated with ATN-224 (25 uM for 24 hours) and stained for Annexin V-APC and PI for apoptosis; multiple unpaired t-tests. **(B–C)** Dose response curves for cell viability with SOD1-inhibitor (ATN-224) **(B)** or ATN-224 in combination with 0.25 uM NAC **(C)** in WT and *PPM1D*-mutant leukemia cell lines after 24-hours. Mean ± SD (n=3) is shown along with a non-linear regression curve. All values are normalized to the baseline cell viability with vehicle, as measured by MTT assay. **(D)** Total reactive oxygen species (ROS)of WT and *Ppm1d*-mutant MEFs measured by DCFDA (10 uM) staining. MFI was determined by flow cytometry. n=6 biological replicates were used for each genotype. Data shown are the mean of each biological replicate; unpaired t-test. **(E)** Total ROS of WT GM12878) and *PPM1D*-mutant patient lymphoblastic cell lines (LCLs) at baseline, and after 24-hrs of SOD1 inhibition measured by DCFDA (10 uM) staining. MFI was determined by flow cytometry**;** multiple unpaired t-tests, **(F)** Dose response curve of WT and *PPM1D*-mutant LCLs after ATN-224 treatment. IC50s of WT and *PPM1D*-mutant LCLs were 48.8 uM and 20.51 uM, respectively as measured by MTT assay; non-linear regression analysis, ns=non-significant (p>0.05), **p<0.01, ***p<0.001, ****p<0.0001.

Figure 3 – Figure Supplement 1

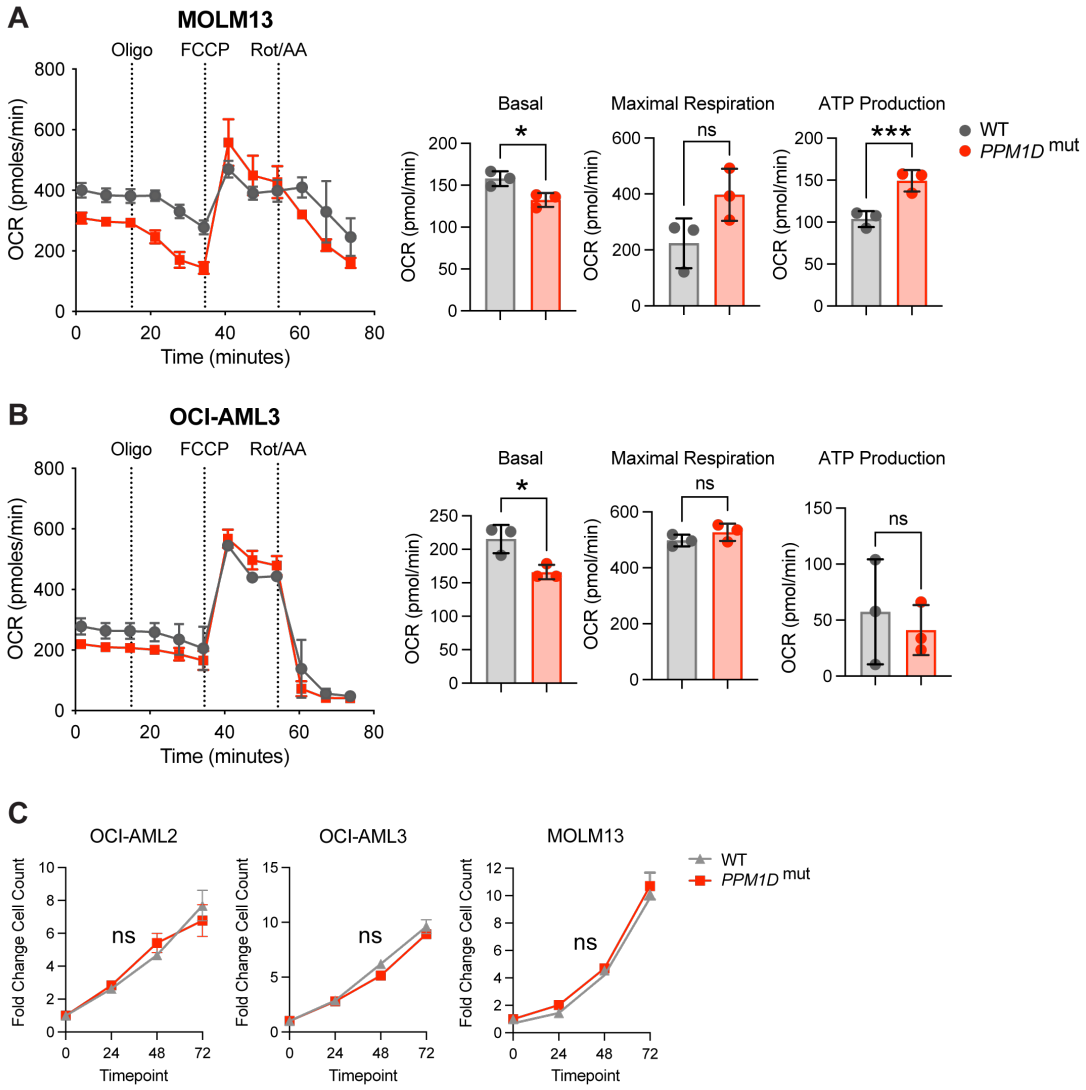

Figure 3 – Figure Supplement 1. *PPM1D*-mutant cells have altered mitochondrial function. (A,B) Measurement of mitochondrial oxygen consumption ratio (OCR) by seahorse assay in WT vs. *PPM1D*-mutant MOLM-13 **(A)** and OCI-AML3 **(B)** cells after treatment with oligomycin (1.5 uM), FCCP (0.5 uM), and rot/AA (0.5 uM). Quantification of basal, maximal, and ATP-linked respiration shown. Each cell line was performed in technical triplicates, student's t-test. **(C)** Growth curves of WT and *PPM1D*-mutant leukemia cell lines at 24-, 48-, and 72-hours. Cell counts were normalized to day 0. ns=non-significant (p>0.05), *p<0.05, ***p<0.001.

Figure 4 – Figure supplement 1

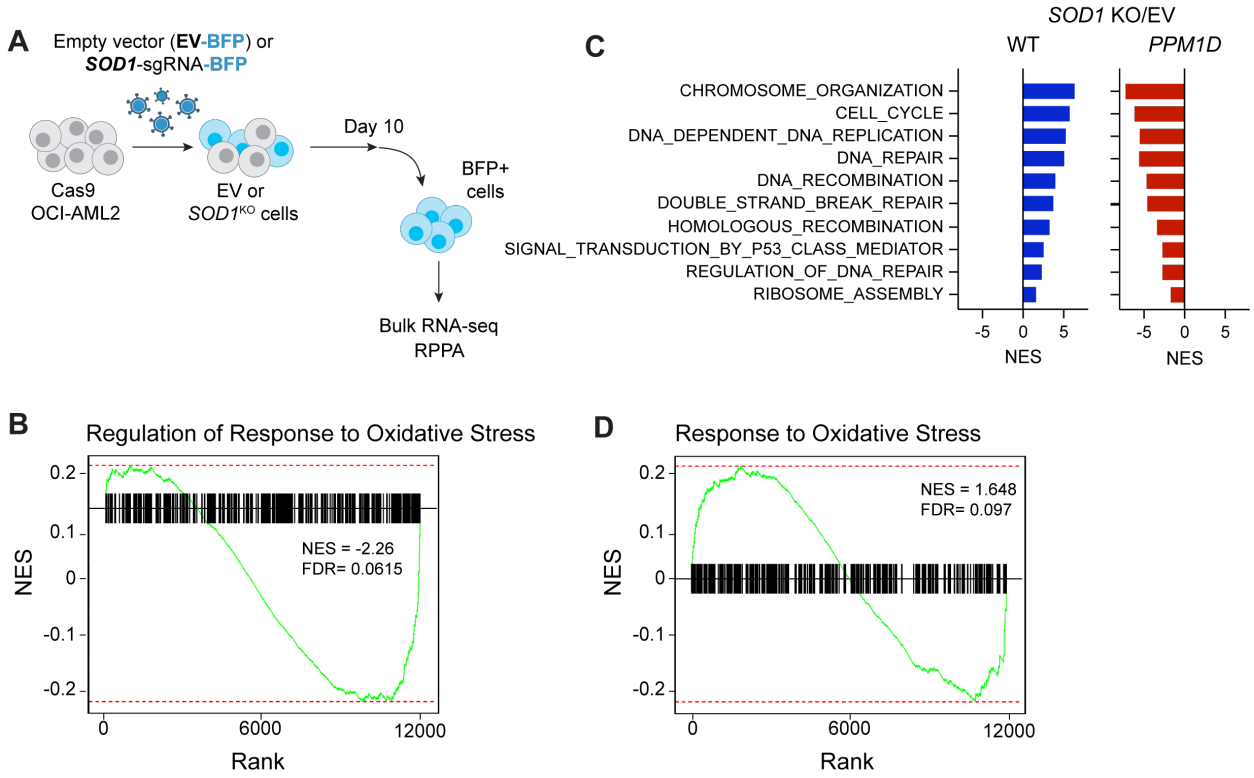

Figure 4 – Figure Supplement 1. *PPM1D*-mutant cells have reduced oxidative stress response. (A) Schematic of the experimental setup for the bulk RNA-sequencing and reverse-phase protein array. WT and *PPM1D*-mutant Cas9 OCI-AML2 cells were transduced with either empty vector (EV)-BFP or *SOD1*-sgRNA-BFP. Cells were passaged for ten days and then sorted for BFP expression for downstream analysis. **(B, D)** GSEA enrichment plots for *PPM1D*-mutant cells compared to WT after transduction with EV **(B)** or after *SOD1*-knockout **(D)** for the "Regulation of Response to Oxidative Stress" (GO:1902882) and "Response to Oxidative Stress" (GO:0006979). NES are shown with FDR<0.25. **(C)** GSEA analysis of RNA-sequencing of *SOD1*-deleted cells compared to EV control in WT and *PPM1D*-mutant cells. Blue and red bars indicate significantly up- and downregulated pathways, respectively. Normalized enrichment scores (NES) are indicated. All pathways filtered for FDR<0.25.

Figure 4 – Figure supplement 2

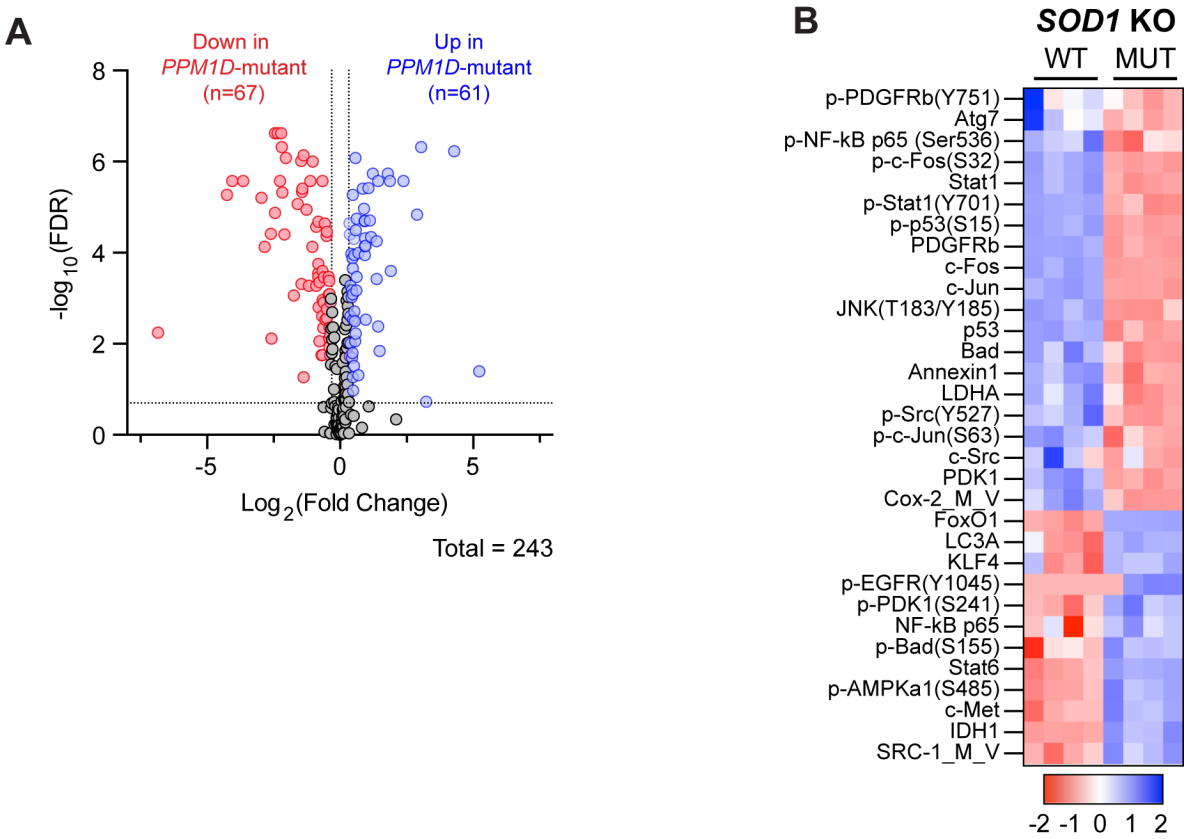

Figure 4 – Figure Supplement 2. *PPM1D*-mutant cells have reduced oxidative stress response. (A) Volcano plot of the differentially expressed proteins from the RPPA in *PPM1D*-mutant OCI-AML2 cells compared to WT. Red and blue dots indicate significantly up- or downregulated proteins, respectively, with a cutoff FDR<0.2 and linear fold change >|1.2|. **(B)** RPPA profiling of WT and *PPM1D*-mutant cells after *SOD1* deletion. Proteins from the "Response to Oxidative Stress" pathway have been selected for the heatmap. Each column represents a technical replicate. See Figure 4-source data 2 for the raw data.

Figure 5 – Figure supplement 1

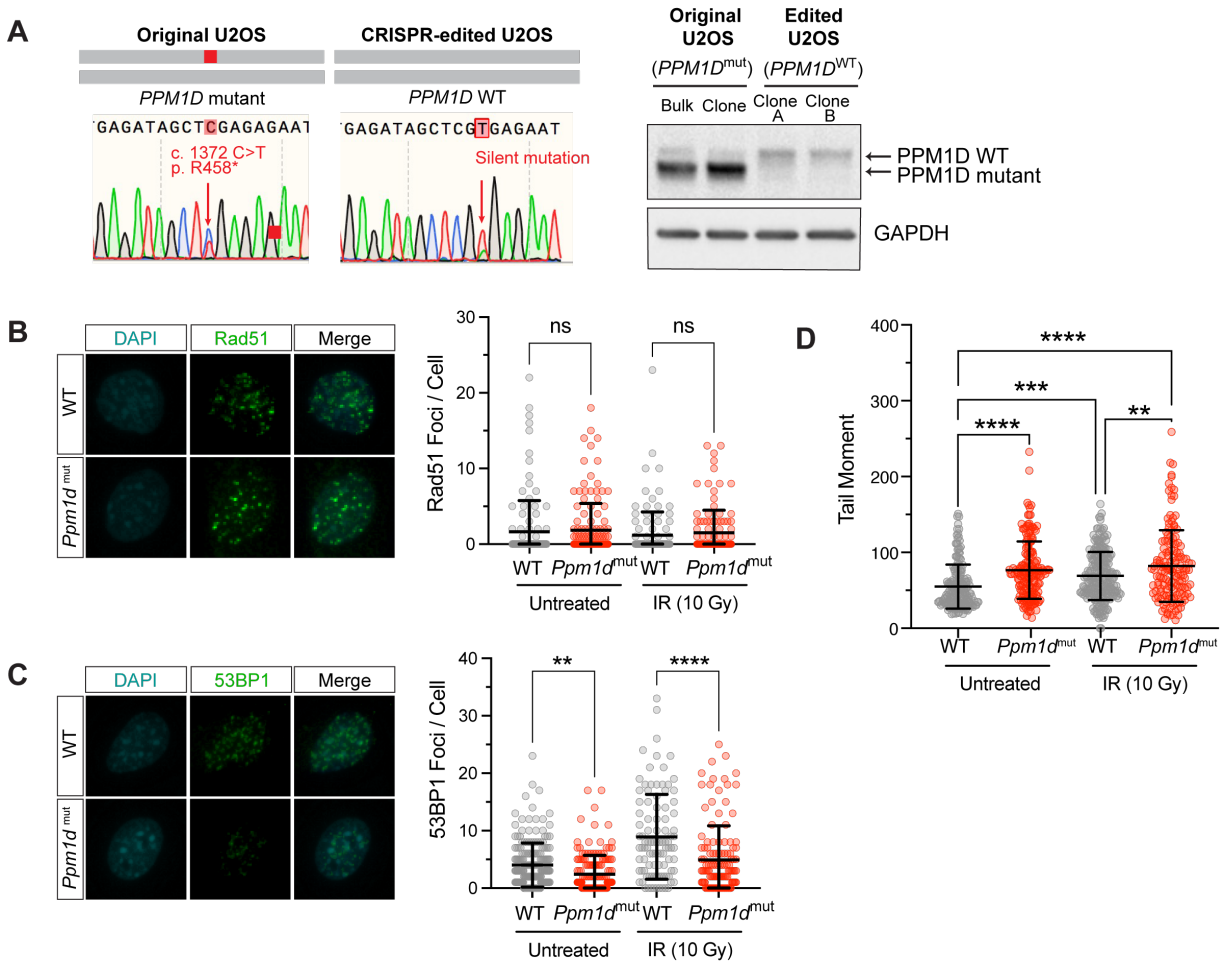

Supplementary Figure 5. *PPM1D*-mutations increase genomic instability and impairs non-homologous end-joining repair. (A) Left: Sanger sequencing traces of the parental U2OS cell line harboring a c.1372 C>T mutation in *PPM1D* and the CRISPR-edited U2OS cell line with mutation corrected to WT PPM1D. Right: Immunoblot validation of these clones are shown. Lysates were probe with anti-PPM1D (1:1000) and anti-GAPDH (1:1000). **(B,C)** Left: Representative images of Rad51 and 53BP1 immunofluorescence microscopy. Mouse embryonic fibroblasts were treated with 10 Gy irradiation, harvested 1-hour post-irradiation and stained for the indicated markers. Right: Quantification of the number of foci per cell is shown. Analysis was performed using CellProfiler. n>100 cells for each condition; students t-test. **(D)** Comet assay quantification of mouse embryonic fibroblasts at baseline and after 1-hour post-irradiation (10 Gy). Quantification and analysis of tail moments were performed using the Comet IV software. n≥150 comets were scored per experimental group; 2way ANOVA, ns=non-significant ($p>0.05$), **$p<0.01$, ***$p<0.001$, ****$p<0.0001$.